Air–liquid interactions in a pressure-swirl spray

JEDELSKÝ, J.; MALÝ, M.; DEL CORRAL, N.; WIGLEY, G.; JANÁČKOVÁ, L.; JÍCHA, M.

International journal of heat and mass transfer
2018, vol. 121, June 2018, pp. 788-804

ISSN: 0017-9310

DOI: https://doi.org/10.1016/j.ijheatmasstransfer.2018.01.003

Accepted manuscript

AIR–LIQUID INTERACTIONS IN A PRESSURE-SWIRL SPRAY

Jan Jedelsky[1], Milan Maly[1], Noé Pinto del Corral[2], Graham Wigley[3], Lada Janackova[1] and Miroslav Jicha[1]

[1]Faculty of Mechanical Engineering, Brno University of Technology, Technicka 2896/2, Brno 61669, Czech Republic, jedelsky@fme.vutbr.cz
[2]Faculty of Sciences, Universidad Autónoma de Madrid, C/Francisco Tomás y Valiente 7, 28049 Madrid, Spain, noe.pinto.delcorral@gmail.com
[3]Aeronautical and Automotive Engineering, Loughborough University, LE11 3TU, UK, g.wigley@lboro.ac.uk

ABSTRACT

The energy transfer between a liquid hollow cone spray and the surrounding air has been studied using both imaging and phase-Doppler techniques. The spray was produced by a pressure-swirl atomizer discharging Jet A-1 fuel at inlet over pressures of Δp = 0.5, 1.0 and 1.5 MPa into quiescent ambient air.

The liquid exits the nozzle as a conical film which thins as it spreads and develops long- and short-wave sinusoidal instabilities with breakup occurring, at the length smaller than that predicted by the inviscid model, to form film fragments and ultimately droplets downstream the spray.

The single shot imaging characterised the spray regions of near-nozzle flow, the breakup processes and the developed spray. The phase-Doppler system resolved the three components of velocity and size for the droplet flow as measured on radial profiles for four axial distances from the nozzle exit.

A Stokes number, *Stk*, analysis of the droplets' response times to the airflow time-scales showed that droplets < 5 μm followed the airflow faithfully and so were used to estimate the local airflow velocity. This allowed a comparison of both the droplet and airflow fields in terms of their mean and fluctuating velocity components to be made.

The formation of the hollow cone spray and the interaction of the fragments and droplets with the air, through viscous drag, induce complex entrained airflows. The airflow was found to be highly anisotropic, fluctuating preferentially in the downstream direction, and spatially varying within three distinct spray regions. The air drag establishes a positive size–velocity correlation of droplets; their *Stk* reduces with axial distance and increases with droplet size and Δp; so that $Stk \approx 1$ for 20–40 μm droplets and the largest droplets (80–160 μm, $Stk > 10$) move ballistically.

The spatially resolved mean and turbulent kinetic energies of the air and spectra of the droplet velocity fluctuations are detailed in the paper. These findings are relevant to scientists and engineers modelling the complex two-phase flows.

KEYWORDS

gas-liquid flow, droplet clustering, hollow-cone spray, air-droplet interaction, Stokes number, droplet dynamics, flow seeding

1. INTRODUCTION

Pressure-swirl (PS) atomizers have been widely used for decades in industrial, domestic, agricultural and other applications. Their principle lies in the conversion of the pressure energy of the pumped liquid into kinetic energy to create a high-speed swirling conical film of liquid which discharges into the surrounding gas (usually air). The film breaks up primarily due to stretching and then to aerodynamic shear forces (Villermaux, 2004). The initial difference between the velocity of the liquid and gas phase induces a strong dynamic liquid–gas interactions. It plays a substantial role in the entire atomization process and influences, or even causes, secondary effects during the spray formation. The high-momentum liquid fragments induce an entrained air motion, which consequently controls the flow of smaller liquid volumes and results in

dispersion and reposition of small droplets downstream (Dikshit et al., 2009), where droplet collisions (J. L. Santolaya, García, Calvo, & Cerecedo, 2013) and droplet clustering (Domann & Hardalupas, 2002) have been seen to occur. The combined contribution of the above regulate the fundamental sprays characteristics, such as spray dispersion angle and droplet size and velocity distributions (Durdina, Jedelsky, & Jicha, 2014). The mutual interaction of the dispersed phase and the gaseous phase is important in both reacting and nonreacting flows where the droplet characteristics and their response to the airflow pattern have, for example, an effect on the flame shape and stability, sooting characteristics, and emission of combustion products (Brena de La Rosa, Wang, & Bachalo, 1990). Also, the character of the turbulence has consequences in the mass transfer applications where the atomization process frequently appears. For example, in reactive and evaporating sprays it causes augmentation of the reactions and mass transfer.

PS sprays contain a wide range of droplet sizes exhibiting different dynamic behaviour. The liquid–gas interaction spatially redistributes the spray droplets due to the size-dependent droplet inertia, momentum, and drag. It was shown for PS atomizers, in the absence of significant external airflow fields, that large droplets tend to maintain the high velocity of the liquid sheet whereas small droplets couple with the local-induced airflow (Bachalo, 2000; Bates, 1994; Zhao, Li, & Chin, 1986). Spraying into co- and cross-flowing air additionally modifies the droplet trajectories with an important effect of droplet size on the outcome (Mellor, Chigier, & Beer, 2013; Sturgess, Syed, & McManus, 1985).

The interaction with the surrounding gas can lead to the local formation of instantaneous clusters of droplets in the flow (Eaton & Fessler, 1994; Zimmer, Domann, Hardalupas, & Ikeda, 2003). Rouson and Eaton (2001) used a direct numerical simulation (DNS) to document two extremes in the dispersed particles' response to turbulence. High-*Stk* particles respond only slightly to turbulent eddies, and their motion lacks mechanisms for non-random clustering. Low-*Stk* particles act as flow tracers and the medium-*Stk* particles tend to segregate into clusters. Katoshevski et al. (2008) investigated droplet trajectories and showed distinctive characteristics of grouping and non-grouping cases with the effect of droplet size on the grouping pattern. Further works, experimentally (Balachandar & Eaton, 2010) and numerically (Soldati & Marchioli, 2009; Zonta, Marchioli, & Soldati, 2013) evidenced that particles in a swirl-free turbulent flow exhibit non-uniform spatial distribution. The degree of non-uniformity is induced by particle–turbulence interaction on the particle scale and depends on particle inertia. The turbulence-driven radial droplet dispersion and reposition can possibly be controlled by the susceptibility for particles to shift in the direction of decreasing turbulence levels (turbophoresis) and by the concentration gradient of the particles, as observed in the DNS study by Lee & Lee (2014). The droplet clustering phenomena was observed in PS sprays (Domann & Hardalupas, 2002; Durdina et al., 2014; Wang, McDonell, & Samuelsen, 1992). Droplets, concentrated in clusters (or packets) make the spray spatially and temporally non-uniform (Dressler, 1993), which is an important issue in combustion applications; the combustion of these clusters can lead to periodic variations in the heat-release rate and pressure in the combustor and, in turn, may result in various problems such as combustion noise or combustion-driven oscillations and low combustion efficiency (Takahashi, Schmoll, & Dressler, 1995).[1]

To summarise the above findings, the dynamic liquid–gas interaction is of principal importance in the PS spray formation process as it affects the atomization as well as the further life of droplets in the consequent processes. The deduction is that the liquid–gas interaction produces the near-field turbulent airflow, and that the air drag establishes a strong positive size–velocity correlation. The turbulent flow can lead to preferential clustering. It is of practical and fundamental interest to elucidate what is the role of ambient air in the motion of the sprayed liquid and what droplet sizes are affected by the drag effect.

The turbulent characteristics of the liquid-induced entrained airflow (spatially resolved turbulent kinetic energy (TKE) and mean kinetic energy (MKE), isotropy and homogeneity, frequency characteristics) and the

[1] Note for completeness that several further mechanisms and forces (e.g. diffusiophoresis, photophoresis, Brownian diffusion) apply in the disperse particle–gas systems, but these act on the particles sized comparably with the gas mean free path (0.07 μm) (Kulkarni, Baron, & Willeke, 2011) and are not apparent in the sprays where droplets above 1 μm are produced.

size range of air-affected droplets can be determined by the analysis of the size-discriminated droplet and gas flow fields and used to elucidate the role of the entrained air in the spray development downstream. Amongst a number of studies on PS sprays, only few deal with the phase-resolved velocity fields; therefore, a detailed measurement of the velocity of both the phases is still required. The ambient flow field is often traced using artificial seeding particles (Brena de La Rosa et al., 1990; J. L. Santolaya et al., 2013; Koyama and Tachibana, 2013; Rottenkolber et al., 2000; Lecourt et al., 2011) or probed with conventional methods (Tishkoff et al., 1982). Since PS sprays contain droplets in a wide size range then the smallest ones could serve as natural tracers. De la Rosa et al. (1990) studied the effect of swirl on the velocity and turbulence fields of PS sprays and observed that, in general, droplets up to 5 μm in diameter responded well to the fluctuations of the air velocity; the turbulence intensity for 5 μm droplets and the air differed only slightly. They concluded that droplets smaller than 5 μm follow the air motion reasonably well. Also, Sanchez et al. (2000) used spray droplets sized under 5 μm as tracers of the gas velocity. However, the concept of the smallest droplets used as natural tracers requires a detailed analysis to be proved and optimised in our case.

This study focuses on a small PS atomizer, intended for a gas turbine. The air–liquid interaction phenomena are addressed and estimates of the spatially resolved flow fields of air and liquid within the spray are made. The turbulence characteristics (spatial, directional and spectral) are qualitatively described, and the main values are quantified. It is based on measurements of droplet size and the three-component droplet velocity using phase-Doppler Anemometry (PDA). The results elucidate the transfer process of kinetic energy from the liquid (droplets) to the air MKE and TKE, the size range of the droplets affected by the air drag and the structure of the turbulent airflow field and the sprayed liquid.

This study aims to improve the current understanding of the PS spray morphology by a comprehensive investigation of the gas-liquid energy transfer with a link amongst different related phenomena that was not found in earlier works. It experimentally provides gas and liquid thermodynamic characteristics of the spraying process and discusses them in the context of previous references. These can be used to validate numerical simulations and show the modellers which phenomena are important to be included in their CFD models to compute realistic simulations.

The focus of the study is the idealised case of a liquid discharged into a quiescent air. It is proposed to extend this study to the cases typical of combusting sprays such as co- and cross-flowing air (Bai, Zhang, Liu, & Sun, 2009; Mellor et al., 2013; Rachner, Becker, Hassa, & Doerr, 2002; Sturgess et al., 1985) or controlled external turbulence (Elbadawy, Gaskell, Lawes, & Thompson, 2015).

Several important phenomena of the spraying process such as secondary droplet breakup, droplet collisions, and liquid evaporation are closely linked to, or influenced by the air–liquid interaction. These phenomena require attention and are not covered by this paper with the aim to keep it focused and not too lengthy. So the results presented here will be used as a base for the following work on these topics.

2. EXPERIMENTAL

This investigation of the air–liquid interaction in the PS spray applies experimental data acquired by optical probing of spray produced by a PS atomizer in the Spray laboratory at the Brno University of Technology. Following paragraphs describe the essential experimental apparatus used including the atomizer under test, the cold-spray test bench with the fluid supply system, PDA and a digital camera with illumination systems.

2.1. Atomizer and test bench

A small PS atomizer, developed for an aircraft engine, was operated continuously in cold-flow (non-reacting) conditions and sprayed aviation fuel Jet A-1 (kerosene) at room temperature, 20 °C, into the quiescent air. The fuel with a density $\rho_l = 795$ kg/m^3, viscosity $\mu_l = 0.0016$ kg/(m·s) and surface tension $\sigma = 0.029$ kg/s^2 was provided at inlet gauge pressures of $\Delta p = 0.5$, 1.0, and 1.5 MPa. All the tests were conducted with one fuel batch. The atomizer was fixed to a 3D computer controlled traverse. Alignment accuracy of the support is 0.2 mm against the measurement volume of PDA system.

The main internal geometric dimensions of the atomizer are shown in Figure 1. Three tangentially arranged inlet channels with rectangular cross-section fed the hemispherically shaped swirl chamber with the pressurised liquid. The swirling liquid discharges through a circular exit orifice with 1:1 length-to-diameter ratio into the air.

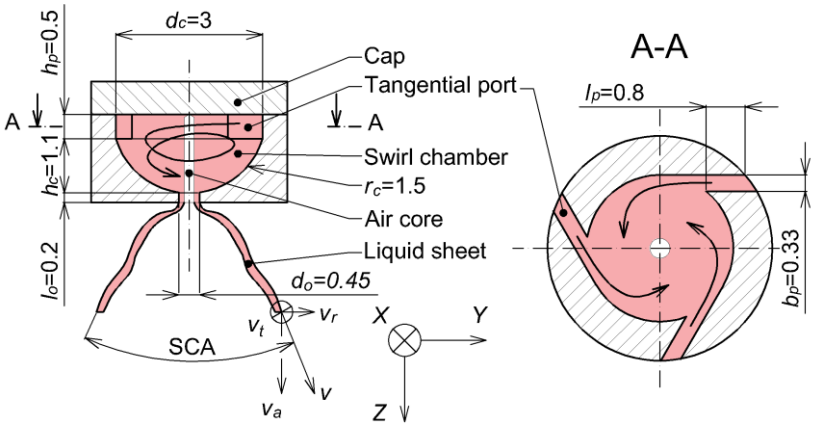

Figure 1. Schematic layout of the atomizer with main dimensions in millimetres: side section with the coordinate system (left) and top section (right).

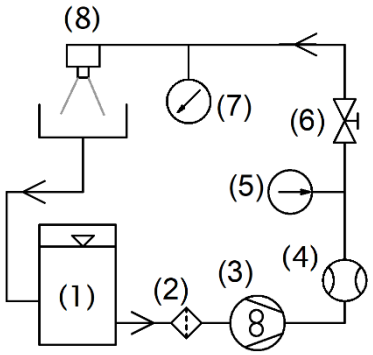

Figure 2. Schematic layout of the experimental facility.

The cold test bench (Figure 2) uses a gear pump (3) to supply fuel from the main tank (1) through filters (2), flow rate, temperature and pressure sensors (4, 5, and 7 respectively) and through a control valve (6) into the atomizer (8). The spray freely falls into a collector and returns into the main tank. The flow rate is controlled by the pump speed and metered by a Mass 2100 Di3 Coriolis mass flow meter fitted with a Mass 6000 transmitter (Siemens AG, DE). The uncertainty of mass flow rate was 0.1% of its actual value, the uncertainty of pressure sensing (DMP 331l, BD SENSORS s.r.o., CZ) was 2 kPa and the uncertainty of temperature sensing (PR-13, OMEGA Engineering, Inc., US) was 0.2 °C.

2.2. PDA and spray imaging

The sprayed droplets were probed using a two-component fibre-based commercial PDA (Dantec Dynamics A/S, Skovlunde, DK), see Figure 3 and Table 1. A multiline Ar–Ion$^+$ laser produced a horizontally polarised light beam with 1W output power. The green (514.5 nm) and blue (488 nm) wavelength components were extracted and used to measure the axial velocity + droplet diameter and radial or tangential velocity, respectively. Both the beams were split into a pair of parallel beams with a separation of 38 mm which were consequently expanded by a 1.98× beam expander and symmetrically intersected using transmitting optics. The frequency of one beam from each pair was shifted by 40 MHz. The intersected beams formed a prolate ellipsoidal measurement volume with the axis length 0.076 × 0.076 × 0.63 mm. The measurement volume length was truncated by a 0.2-mm wide spatial filter. The positioning of the receiving optics at 70° from the forward direction was used to collect the light scattered from droplets dominated by the first order of refraction and to minimise reflections. Thus, the errors associated with trajectory ambiguities due to the Gaussian beam effect were reduced (Bachalo, 2000).

The point-wise PDA measurements of the time-resolved size and velocity of the individual droplets were performed in four sections of the spray at axial locations from the exit orifice of Z = 12.5, 25, 37.5, and 50 mm on two radially orthogonal axes. The radial traverses were divided into intervals proportional to the

axial distance as $\Delta r = 1/12.5\ Z^2$. In each of the axial locations, two radial axes with 25 positions on each axis, where $r \in (-12, -11, \ldots, 12)/12.5\ Z$, were measured, and 100,000 data samples or 60 seconds data acquisition were taken in every position. Two consequent measurements with simultaneous acquisition of axial + radial and axial + tangential velocity component pairs were provided to obtain all the three orthogonal components for further analysis. The PDA measurements provided validation rates of 60–80% for velocity and 65–95% for droplet size.

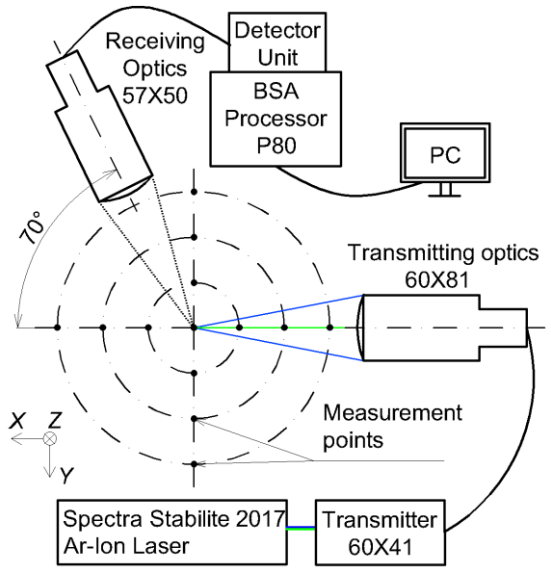

Figure 3. A setup of the PDA with the coordinate system.

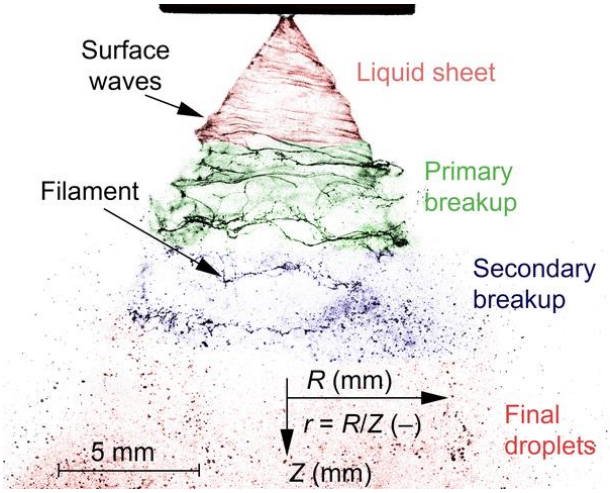

Figure 4. Near-nozzle spray morphology.

Table 1. Main system parameters of the PDA, typically used settings.

Parameter	Value	
Focal length of transmitting lens (mm)	310	
Focal length of receiving lens (mm)	800	
Mask	B	
Velocity component	Axial	Radial, tangential
Wavelength (nm)	514.5	488
Velocity centre (m/s)	8	0
Velocity bandwidth (m/s)	32	30
PM Sensitivity (V)	800	1000
Processor SNR (–)	0	0
Signal gain (dB)	20	20
Level validation ratio (–)	8	2

[2] Relative radial position $r = R/Z$ is often used here instead of the radial position, R, to allow for a convenient comparison of results in different axial distances Z, assuming the simplification that droplets move along direct trajectories with origin in the exit orifice.

A single-shot imaging technique with a back-lit illumination (shadowgraphy) was used to visualise the liquid film and provide details of the breakup processes (Figures 5 and 11 below). A pulsed light sheet served for a cross-sectional illumination of the spray to observe the droplet and bulk-liquid structures inside the spray cone (Figures 11 and 15 below) using Mie scattering. All the shadowgraphy and Mie scattering images were taken from a distance of 20 and 50 mm to the atomizer axis by Canon EOS 70D camera with Canon EF 100 mm f/2.8 USM Macro lens fitted to a 68-mm long extension tube. The camera settings were: ISO 400, aperture f/11, shutter speed 1/2 s for shadowgraph imaging and ISO 100, aperture f/5, shutter speed 1/2 s for the sectional imaging, respectively. The back-lit illumination used a pulsed laser beam from a Nd:YAG Gemini laser (New Wave Research, Inc, US) which was first expanded by a microscope objective and then diffused by projection onto a ground glass plate. The beam had a 532-nm wavelength, a duration of 5 ns and energy of ≈ 20 mJ. The pulsed light sheet was produced by the same Nd:YAG laser but equipped with a cylindrical lens. The light sheet, with a thickness of 1 mm, illuminated the spray from the side while the camera observed the spray section at 90°angle to the sheet.

3. RESULTS AND DISCUSSION

The internal flow and primary breakup strongly affect the spray formation downstream and therefore need to be discussed to some extent. As the nozzle is too small for flow visualization inside the swirl chamber, the character of the flow inside the swirl chamber was estimated using simple calculations and the "external" findings. Descriptions of the spraying process are based on the near-nozzle photographic observations and the PDA measurements in the developed spray.

3.1. Liquid discharge, sheet formation, and primary breakup

The liquid, pumped under pressure through the tangential inlet ports, swirls inside the nozzle and discharges from the exit orifice with a high velocity into, initially low turbulent, quiescent air (Figures 1 and 4). The internal flow Reynolds number (Walzel) $Re_W = \sqrt{2\rho_l \Delta p}\, d_o / \mu_l$ ranges from 7930 to 13735 (see Table 2) and exceeds the critical value for turbulent transition $Re_{Wc} = 5000$ (Walzel, 1993) and therefore suggests that the flow is fully turbulent[3].

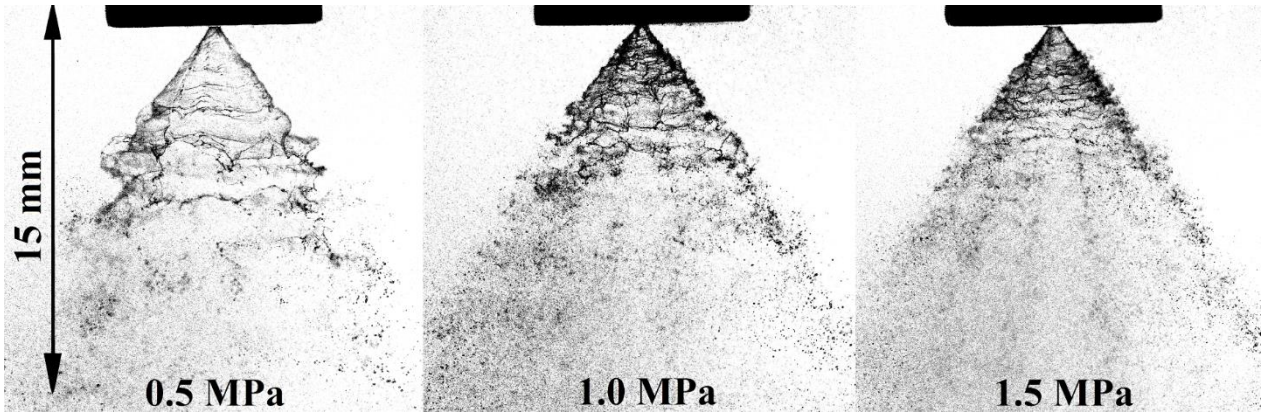

Figure 5. Breakup process of the discharged liquid sheet.

The Δp range determines the nozzle operation in the region where the discharged liquid forms a thin conical sheet (see Figure 5); its thickness at the nozzle orifice is, as common for low viscosity liquids, almost constant over the pressure range studied: t_o = 70–75 μm (Table 2). It agrees with the prediction of Giffen and Muraszew (1953) for nonviscous fluids (73 μm) and Lefebvre and Suyari (1986):

[3] Some authors assume the flow to be laminar even for higher *Re* (Yule and Chinn (1997) up to *Re* = 50,000) also because, inside the swirl chamber, the radial forces of the swirl tend to laminarise the flow (Chinn, 2008).

$$0.735C_D^2 = \frac{(1-X)^3}{1+X} \qquad (0)$$

where the ratio of the area of the air core to the area of the final discharge orifice $X = (d_o - 2t_o)^2 / d_o^2$. Eq. (1) results in t_o = 74 μm while other, often more complex, equations give a much worse agreement.

The formation of the annular liquid structure through the exit orifice features a relatively low discharge coefficient, C_D. It is almost independent of the pressure drop (see Table 2) and in reasonable agreement with the prediction of Rizk and Lefebvre (1985): $C_D = 0.35\left(\frac{A_p}{d_c d_o}\right)^{0,5}\left(\frac{d_c}{d_o}\right)^{0,25} = 0.39$. Here A_p is the cross-sectional area of swirl ports, d_o exit orifice diameter and d_c is swirl chamber diameter. The efficiency of the conversion of inlet potential energy into kinetic energy at the nozzle exit is

$$\eta_n = \rho_l v_o^2 / 2\Delta p \,. \qquad (0)$$

This so-called nozzle efficiency was estimated approximating from the PDA data for the velocity of the liquid phase in the axial distance from the exit orifice Z = 6 mm to the velocity of the liquid at the orifice, v_o. The results of η_n = 0.34–0.41 (Table 2) are rather low, if compared with other authors. Horvay with Leuckel (1985, 1986) found η_n = 0.42–0.66 depending on the shape of the convergent part of the swirl chamber and Yule with Chinn (2000) reported for large PS atomizers η_n = 0.73–0.86. The difference can be explained by the small scale of the atomizer used and hence a large friction loss during the internal flow when the area of the inner surfaces is large compared to their volume.

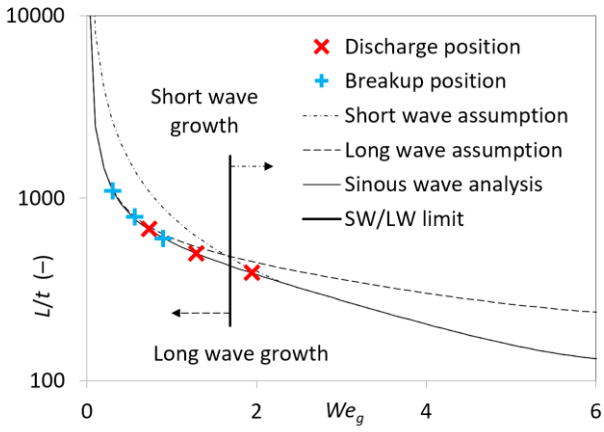

Figure 6. Predicted dimensionless breakup length as a function of We_g for the general, inviscid sinuous, long-wave and short-wave modes, according (Senecal & Schmidt, 1999) with the addition of the present data.

The thickness of the conical liquid sheet decreases downstream from the nozzle. A strong dynamic liquid–gas interaction results from the high-velocity shear between the discharged liquid sheet and the surrounding air and produces instabilities in the sheet of the Kelvin–Helmholtz type. Turbulent perturbations are induced on the swirling motion inside the chamber aid to produce sheet deformations. The ratio between the disrupting gas forces and the consolidating surface tension forces of the liquid film is expressed by the gas Weber number, $We_g = \rho_g v_l^2 \, t / 2\sigma$, where the indices g and l stand for gas (air here) and liquid respectively.

Table 2. Basic characteristics of the flow and spray

Δp	$\dot{m}_l$	C_D[a]	η_n[b]	Z_b[c]	t_o[d]	SCA[c]	e_A[e]	ID_{32}[f]	η_a[g]	We_{go}	Re_W
MPa	kg/h	–	%	Mm	μm	deg	%	μm	%	–	–
0.5	5.4	0.33	41	4.1	70	75	0.21	53	0.65	0.73	7930
1.0	7.3	0.32	34	3.6	74	79	0.11	42	0.42	1.29	11215
1.5	9.0	0.32	34	3.0	75	82	0.07	38	0.31	1.94	13735

[a] $C_D = \dot{m}_l / A_o \sqrt{2\rho_l \Delta p}$, where $\dot{m}_l$ is the liquid mass flow rate and A_o is the cross-sectional area of exit orifice

[b] calculated according to Eq. (2)

[c] based on the near-nozzle spray photography

[d] $t_0 = d_o \left(1 - \sqrt{1 - C_D/\eta_n}\right) / 2$

[e] $e_A = E_A / E_i = 2\sigma / t_b \Delta p$

[f] the ID_{32} is the "integral" D_{32} over all radial profile and it is calculated according to Eq. (A.2) in (Jedelsky & Jicha, 2014) from PDA drop-size data for Z = 50 mm

[g] calculated according to Eq. (8) in (Jedelsky & Jicha, 2014)

A critical Weber number We_{gc} = 27/16 (Senecal & Schmidt, 1999) determines whether long-wave or short-wave growth dominates the process; long waves prevail when $We_g < We_{gc}$ and short waves in the opposite case. The actual gas Weber number $We_{go} = 0.7 - 1.9$ (see Table 2) at the discharge orifice position reduces to $We_{gb} = 0.3 - 0.9$ at the breakup point. This, in comparison with We_{gc}, shows that the atomizer operation points are placed just below the transition from a long-wave to short-wave growth and the sheet should breakup namely due to the long-wave instability of sinuous mode[4] (Figures 5 and 6). The long-wave sheet instabilities are evident in Z = 3–4 mm for the regime at Δp = 0.5 MPa and start up even earlier for increased Δp (see Figure 5). The length of the wavelet structures significantly reduced when Δp reaches 1 MPa (and thereby a higher We); in such a case, short-wave instabilities begin to be responsible for the sheet breakup in agreement with other experiments (Ramamurthi & Tharakan, 1998). However, it is inconsistent with theoretical models.

The sheet oscillations are amplified, forming waves that distort later downstream. The mutual interaction of the sheet with surrounding air becomes more intense in terms of momentum exchange and entrainment as the sheet momentum reduces due to the film thinning. It yields an increase of the surface energy of the liquid sheet, and, when the local sheet thickness reduces to a critical value, the action of surface tension forces on the perturbed sheet generates perforations. The sheet disrupts or tears into fragments at the breakup distance of Z_b = 3–6 mm (see Table 2 and Figure 5) when the average breakup thickness $t_b \approx 32$ μm regardless of Δp. Most of the inlet energy in this stage is dissipated by the internal flow losses, about 1/3 is kept in the kinetic energy of the liquid fragments, and only 0.2–0.07% (see Table 2) is transferred to the created liquid–air interface. The actual breakup length L_b = 4–5 mm is smaller than the length predicted using the inviscid model for our data at both the discharge and the breakup positions (for the discharge conditions, e.g., L_b = 14.7–23.7 mm theoretically). Note that larger L_b would have allowed the liquid sheet to diminish more before the breakup and would have resulted in smaller droplets.

The model assumes a spectrum of infinitesimal disturbances imposed on the initially steady motion of the liquid film. The internal flow is naturally turbulent and complex for the Re range studied (see Table 2), and the internally induced disturbances have a finite and sufficiently high value so that the emerging liquid sheet is turbulent or transitional from the beginning. The instabilities produce fluctuating velocities and pressures in the flow. In a real case, and, especially, if the excitation frequency corresponds to the frequency of the most unstable mode, these disturbances could reduce the breakup length. It explains the difference between theoretical and real L_b values as well as the transition from long-wave to short-wave instabilities before We_g reaches We_{gc}. This reasoning is supported by the work of Sharief et al. (2000) who hypothesised that primary atomization in the solid-cone PS sprays depends on the turbulence characteristics inside the atomizer. Yule and Chinn (2000) documented the occurrence of the internal secondary motion (particularly Görtler vortices) inside a swirl chamber of a PS atomizer and identified it as a possible source of air-core surface waves. These authors indicated that such perturbations could influence the sheet and its breakup downstream. Also,

[4] Note for completeness that the varicose mode, typical for gas–liquid density ratios ρ_g/ρ_l near unity, does not participate in our case as also confirmed with the near-nozzle visualisations (Figure 5 and other images not included here).

Ma (2000) and Marchione et al. (2007) concluded that the turbulence and unsteadiness in the internal flowfield is the main reason influencing the properties of the sheet formed at the orifice exit and the dynamics of the spray. This behaviour, though, contradicts numerical findings of Deng et al. (2016).

The primary breakup process continues with a rapid contraction and ordering of the detached sheet fragments into irregularly shaped unstable filaments (detectable in Figure 5, regime Δp = 0.5 MPa, as thin horizontal filaments in the primary breakup region). These, due to the capillary instability (Villermaux, 2004), break down later into single droplets to form the hollow-cone spray. The relative importance of internal viscous and surface tension forces during the sheet disintegration can be judged by the ratio *We* and *Re* of the liquid phase at the nozzle exit according to Yule and Dunkley (1984): $We_{lo}/Re_o = v_o \mu_l / \sigma$ which increases from 1.3 at Δp = 0.5 MPa to 2 at Δp = 1.5 MPa. It suggests a moderately higher importance of the viscosity at this spray formation stage.

The original two-dimensionality of the sheet breaks down at a short distance downstream from the orifice. The sheet oscillations and mixing with the air result in the radial redistribution and dispersion of the liquid fragments and droplets according to their size classes. The spray acquires the Gaussian velocity profile normal to the sheet surface (Liu, 2000).[5] Also, the arrangement of droplets, determined originally by the position in the filament before its breakup, rapidly changes to a random spatial occurrence due to mixing with the air.

The liquid sheet interacts with the air inside its cone, which allows establishing a recirculation zone along the continuous part of the sheet. This phenomenon and other airflow structures are detailed in Appendix A.

Axially oriented streaks of droplets were detected in the spray images in Figure 5, namely for the 1.5 MPa regime. Such streaks were documented in the PS spray of Nakayama and Ohono (1978) and by Rashad et al. (2016), however, without any comment. Guy (2008) addressed the issue of streakiness in fuel sprays in detail; he identified the fuel streaks as the spray areas of high local fuel concentrations. This meaning of streaks or voids was also found in other papers (Simmons & Harding, 1981; Wang & Lefebvre, 1987a; Wang & Lefebvre, 1987b) where the streak absence was considered to be a proof of excellent spray symmetry. Yule & Widger (1996) used the "streakiness" term to describe the non-uniformities in the liquid distribution in the spray due to the low number of swirling inlets. Note for completeness that similar, but finer and numerous streaks are frequently observed in the sprays from high-pressure swirl automotive injectors (e.g. Park et al., 2009; Wang et al., 2007; Guo, 2015), though their reason may differ. We conclude that the observed streaks are indicative of a circumferentially heterogeneous distribution of the liquid at the exit orifice and can result from geometrical imperfections of the exit orifice or inlet swirling ports, which are difficult to avoid during fabrication of such small-sized atomizers.

3.2. Size-discriminated droplet velocity

The moving liquid film, fragments, and droplets experience mechanical interactions with the air through a viscous drag. The droplets, moving with a very small *Re* (in all cases the droplets show *Re* < 100), are decelerated according to Stokes' law as $dv_p/dt = -18\mu_g (v_p - v_g) / \rho_l d_p^2$ [6], establishing a positive size–velocity correlation. The energy transfer from the liquid phase to the air continuously forces the air in the direction of the droplet motion with the addition of a "turbulent" term caused by shearing of the air. The size-resolved variation in droplet velocity is documented in Figure 7, which correlates the size of droplets with their axial velocity. It also documents a wide size range of the droplets produced: from submicron to more than 70 μm. The following three size ranges can be identified: small droplets with d_p < 20 μm having a low velocity, medium size droplets (20 μm < d_p < 50 μm) that show a positive size–velocity correlation and

[5] The primary breakup process of the conical liquid sheet described above corresponds to the wave disintegration mode as defined by Fraser et al. (1953, 1962) while the rim or perforated-sheet disintegration modes do not apply due to relatively low viscosity and low surface tension of the Jet A-1 fuel.

[6] We neglect the other forces possibly acting on the droplets, such as gravity, stochastic force that accounts for Brownian collisions of the droplet with surrounding fluid molecules, or Basset force.

the largest droplets with a high and size-independent velocity. The smallest droplets match the airflow in a short distance including its fluctuations (see the theoretical response curves for 20 µm sized droplets in Figure 18 below). They are 3–5 times slower (Figure 7) relative to the largest droplets and may contribute to droplet collisions and coalescence in the dense spray region (J. L. Santolaya et al., 2013). The upper size limit of the decelerated droplets extends with distance downstream. The momentum transfer gradually affects all size classes, so even the largest droplets lose their kinetic energy at large downstream distances. It can be judged by comparing the liquid velocity along the droplet trajectory at different downstream positions in Figure 12 below. The air–droplet interaction leads to a size-dependent droplet radial redistribution: small droplets are transported with air from the outer spray zone into the spray centre while larger droplets move on a ballistic trajectory; this behaviour was observed on the spray images. As a consequence, the small particles are missing at the spray periphery, and no airflow tracing is possible there. The issue of droplet response in the airflow is addressed in Section 3.3.

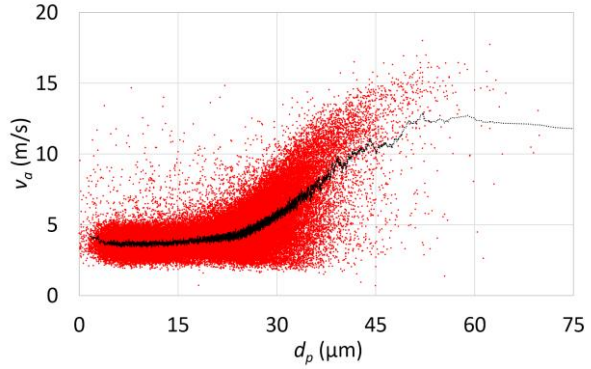

Figure 7. Correlation between size and axial velocity of individual droplets; 100,000 samples, black line represents the flowing average per 100 droplets, Z = 37.5 mm, R = 15 mm, Δp = 1 MPa.

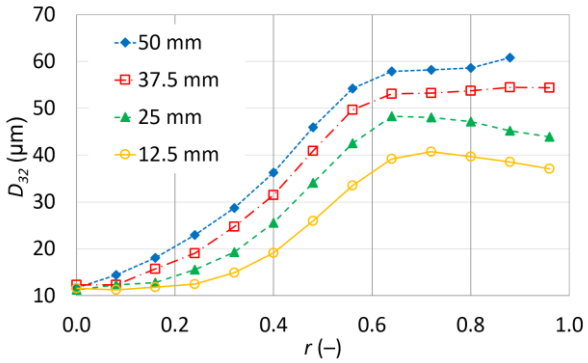

Figure 8. Radial profiles of D_{32} at different Z positions, Δp = 1 MPa.

For convenience, the entire size distribution can be represented at each position with a single mean droplet diameter, whose general definition is:

$$D_{ab} = \sqrt[a-b]{\sum_{i=1}^{n} d_i^a \Big/ \sum_{i=1}^{n} d_i^b}\ , \qquad (0)$$

where d_i represents the diameter of individual droplet i and n a total number of the droplets at the position. For example, D_{10} stands for the arithmetic mean diameter and D_{32} for volume/surface mean diameter[7]. Figure 8 shows a very low mean size, D_{32} < 15 µm, at r = 0 for all axial positions, increasing to D_{32} = 40 µm at high r distances for Z = 12.5 mm and to even larger sizes further downstream. This character of the variation of D_{32} with radial and axial locations agrees well with other observations (Mellor et al., 2013; Sturgess et al., 1985; Zhao et al., 1986). An increase in the droplet size with axial spray development suggests a liquid evaporation of the smaller droplets, a collision driven droplet coalescence, or the breakup of liquid fragments is still taking place to generate droplets and modify their size downstream. A similar trend in the axial and radial size variation was found for D_{10} (see Figure 16 below). Illustrative results, shown in Figures 7 and 8, were discussed here but the features pointed out are qualitatively valid also for other spray positions or pressure regimes.

[7] Also called the Sauter mean diameter and frequently used in mass and heat transfer spray studies.

3.3. Stokes number of droplets

The intensity of interaction of droplets with a surrounding media can be explained by means of the *Stk*, a dimensionless criteria established for the description of the behaviour of particles subjected to a flow. The *Stk* is defined as the ratio of the characteristic time of a particle (or a droplet here) to a characteristic time of the flow and can be in the spray estimated as:

$$Stk = \rho_l C_c \overline{D}_p^2 \Delta\overline{v} \big/ 18\mu_g L\,, \qquad (0)$$

where μ_g is the air dynamic viscosity, and ρ_l is the particle density (the liquid phase density). The characteristic length, L, represents the distance from the breakup position to the reference point $L = \sqrt{Z^2 + R^2} - \sqrt{Z_b^2 + R_b^2}$ and $\Delta\overline{v} = \left|\overrightarrow{v_p} - \overrightarrow{\overline{v}_g}\right| = \sqrt{\left|\left(v_{px} - \overline{v}_{gx}\right)^2 + ...\right|}$ is the difference, in absolute terms, between the local mean air velocity vector[8] and the mean velocity vector of the droplets. The value for $\Delta\overline{v}$ was taken as the average value of the velocity difference along L. The C_c is the Cunningham correction factor and it is ≈ 1 for the droplet sizes in our case. The droplets were sorted out into several size bins with an average diameter in each bin j: $\overline{D}_{pj} = D_{20\,j} = \left(\sum_{i=1}^{n} d_{pij}^2 \big/ n_j\right)^{1/2}$[9], according to Eq. (3).

The *Stk* in the bins increases significantly with $\overline{D}_p$, while the effect of radial position in the spray is minor, see Figure 9.[10] Droplets sized in the range $2.5 \le d_p < 5$ μm move with a very low $Stk \approx 0.02$. Generally, droplets with $Stk << 1$ follow the airflow faithfully[11]. Therefore, the velocity of droplets with $d_p < 5$ μm was used to provide an estimate of the local airflow velocity, v_g. This size range, with $\overline{D}_p = 4\,\mu\text{m}$ typically, corresponds well with the size of seeding particles used in airflow studies by other authors[12].

However, a low *Stk* is not the only requirement that the small spray droplets must obey to suit as natural airflow tracers. Their sufficient number and frequency are required for statistical robustness and the possibility to obtain spectral velocity characteristics, respectively. The former requirement is fulfilled using a sufficiently long duration of the measurement and the latter is conditioned with a high data rate and droplet size distribution with sufficient proportion of small droplets. These conditions were not accomplished for all positions in the PS spray; for example, the outer area contains an insufficient concentration of low-*Stk* particles and so the air entrainment, and external airflow cannot be discerned. Artificial seeding of this area (e.g. Koyama and Tachibana, 2013; Rottenkolber et al., 2000; Lecourt et al., 2011) is advised.

Small droplets are often generated as satellite droplets (Brenn & Kolobaric, 2006) and can be entrained in the wake behind the larger ones. In such a case, their velocity would be biased against the velocity of the ambient gas. We investigated the trend in the velocity of the small droplets ($d_p < 5$ μm) closely following large droplets ($d_p > 20$ μm) according to the time period and the distance between them. We found a negligible velocity–distance correlation which proved that there was no wake effect on the small tracers. Also, Eq. (4) for the *Stk* estimation considers a single droplet subjected to the flow. The forces with which the surrounding fluid acts on the droplets are expressed in terms of the drag coefficient, C_d, which, for a single rigid droplet, depends only on the *Re* (Frohn & Roth, 2000); but in the interacting droplet system it

---

[8] Taken from measurements in *X*, *Y* and *Z* directions.

[9] Where d_{pi} is the diameter of an *i*-th droplet where $i = 1,\ 2,\ \ldots n$; for each size class: $d_{p\min} \le d_p < d_{p\max}$ and $d_{p\max} \big/ d_{p\min} = 2$.

[10] Note that only one-half of the full radial profile is shown here and thereafter for the sake of conciseness as the spray can be considered to be axisymmetric.

[11] Tracking accuracy errors are below 1% for $Stk < 0.1$ according to Tropea et al. (2007).

[12] For example Santolaya et al. (2013) in a similar case generated aerosol with $D_{10} = 3.4$ μm.

varies with the droplet concentration or interdroplet spacings (Poo & Ashgriz, 1991) and depends on the turbulence character (S. Lee, 1987). The extent of interactions between droplets has been given up to seven droplet diameters parallel to the airflow and two droplet diameters normal to the airflow (Poo & Ashgriz, 1991). Based on the PDA data in this work this condition practically does not apply although the spray contains macroscopically dense regions and droplet clusters (see Section 3.6). Therefore, the C_d of the small, accompanied droplets is not modified so significantly from the value for an isolated droplet, to affect *Stk*. Moreover, an order of magnitude change rather than an exact *Stk* value determines the character of the droplet-gas interaction (Sirignano, 2000).

Droplets in size bin 20–40 µm with $Stk \approx 1$ are still somewhat affected by the airflow while the largest droplets (80–160 µm) with $Stk > 10$ move almost ballistically. It is well known that the ambient turbulence increases C_d, (Poo & Ashgriz, 1991); therefore, the *Stk* of droplets of all sizes is rather overestimated in high-turbulent spray regions. The overall data inspection shows that the *Stk* decreases systematically with the axial distance for all size groups. Only two size groups are displayed in Figure 10 for clarity. The *Stk* reduces ≈ 7

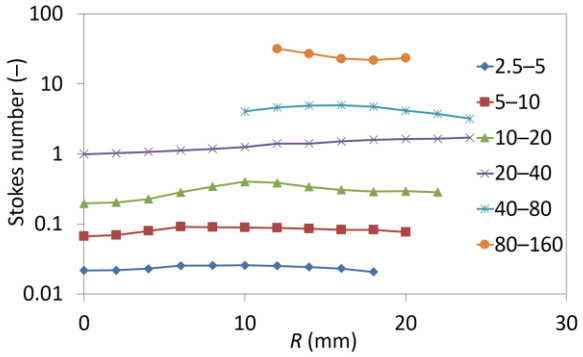

Figure 9. Radial profiles of droplet *Stk* in six size bins (indicated in µm); $Z = 25$ mm, $\Delta p = 1$ MPa. Only positions with more than 80 droplets are displayed.

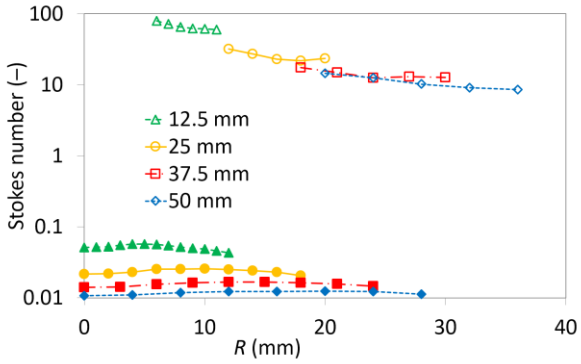

Figure 10. *Stk* of droplets in size bins 2.5–5 µm (full symbols) and 80–160 µm (empty symbols); at the four axial distances, $\Delta p = 1$ MPa.

times with the axial position changed from 12.5 to 50 mm as a consequence of increasing L (included in Eq. (4)) and decreasing $\Delta\bar{v}$. All the *Stk* features found for $\Delta p = 1$ MPa are also valid for the 0.5 and 1.5 MPa values. The *Stk* levels increase moderately and systematically with Δp so that the corresponding *Stk* values for $\Delta p = 1.5$ MPa are approximately 1.8 times higher than those for 0.5 MPa. It is a direct consequence of the proportionality of discharge velocity to Δp and using Eq. (2) gives $v_o = \sqrt{2\eta_n \Delta p / \rho_l}$. The $\Delta\bar{v}$ is proportional to v_o and applying this in Eq. (4) results in $\mathrm{Stk} \sim \bar{D}_p^2 \sqrt{\eta_n \Delta p}/L$, which explains the experimentally observed dependence of *Stk* on Δp.

3.4. Spray structure

The morphology of the sprayed liquid was characterised using backlit and light-sheet illuminated images which were combined in Figure 11. The back illumination emphasizes the large liquid structures, such as the liquid sheet, ligaments and large droplets while the light-sheet crossing the spray centreline uncovers the spray core. The breakup of the conical liquid sheet results in a stream of large droplets in the sheet direction and a number of small droplets positioned inside the spray cone. The externally placed large droplets form a conically shaped spray boundary, with a spray cone apex angle, SCA, increasing from 75 to 82° when Δp increases from 0.5 to 1.5 MPa (see Table 2). The SCA varies as a consequence of the pressure-dependent liquid swirl inside the atomizer. Increasing Δp also promotes the atomization forces, so the ID_{32} reduces from 53 to 38 μm, but the atomization process becomes less effective, as shown by the atomization efficiency, η_a, dropping down from 0.65 to 0.31%.

The sheet illumination images document the absence of small droplets in the outer spray part and their accumulation in the spray centre. Agglomeration of small droplets in some areas (discussed later in Section 3.6) can be detected. Also, large droplets are found nonuniformly distributed as remnants of the liquid structures that were formed during a primary breakup. Both the image sides show no significant development of the spray structure behind the breakup region.

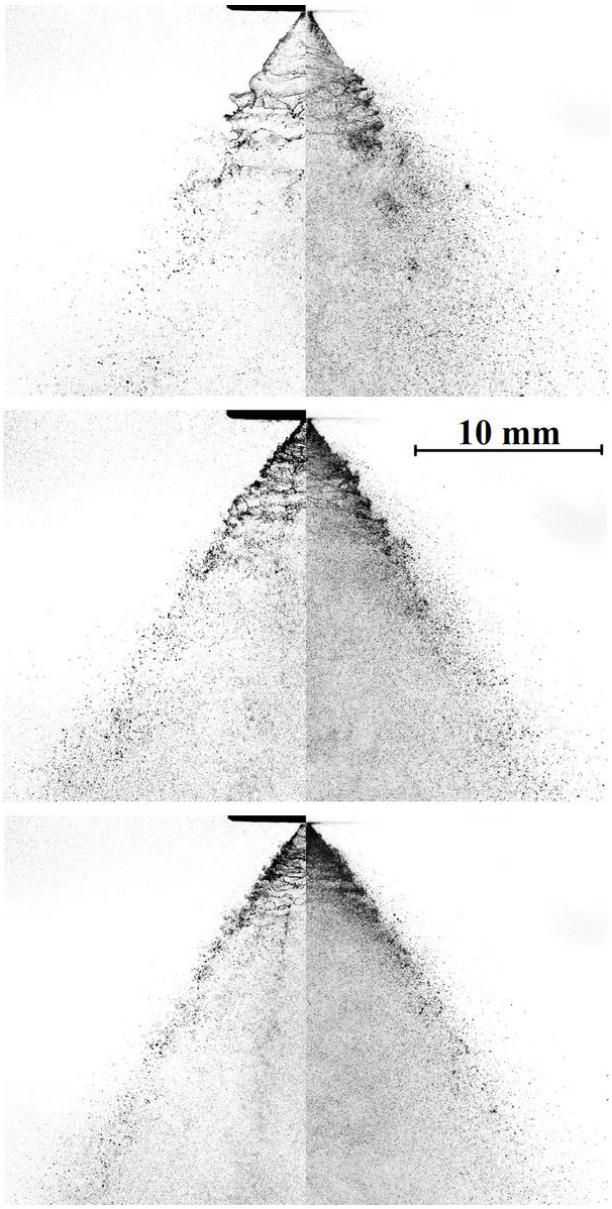

Figure 11. Spray structure, backlit image (left) and light-sheet illuminated image with inverted light scale (right), Δp = 0.5, 1, 1.5 MPa (top to bottom).

3.5. Liquid and gas velocity fields

The volume-averaged droplet velocity was used as a representation of the mean velocity of the liquid mass in the spray:

$$v_l = \sum_{i=1}^{n} d_{pi}^3 v_{pi} \Big/ \sum_{i=1}^{n} d_{pi}^3 \qquad (0)$$

in the axial, radial and tangential directions, with respect to the nozzle mean axis, and it represents the liquid momentum. The velocity field of the liquid mass is compared with the gas velocity field in the combined Figure 12 where the velocity is decomposed to the temporal mean term (indicated below as “mean” only, and shown as vectors) and to the root-mean-square fluctuating term (indicated below as “rms” only, and shown using lines). The radial position, R, in mm is used in Figure 12 for the spatial conformity with the spray shape (Figure 11); but, for the sake of simplicity, the results are described in terms of r (dimensionless), see footnote 2.

The radial distribution of the mean liquid velocity magnitude at Z = 12.5 mm shows a single peak profile with the maximum in the liquid sheet direction which corresponds to other observations of hollow cone sprays (J. Xie et al., 2014). The liquid velocity gradually decreases both to the spray periphery and to the spray centreline due to the interaction with air. The radial profiles are self-similar amongst all the four studied Z distances with the maximum next to the

sheet position (which corresponds to the position of the maximum liquid flux at $r \approx 0.5$). The constant ratio between the mean axial and radial components demonstrates a straight-line movement of the liquid mass from the discharge area. The axial component reaches its local maximum near the positions of the maximum liquid flux. The radial component increases with r from near-zero values at spray centre to its maximum at $r \approx 0.6$ and then slowly decreases in the outer spray; its maximum value is roughly one-half of the axial maximum. The entire flow fields are similar in nature amongst all three pressure regimes. The velocity decays due to momentum transfer from the liquid phase into the originally quiescent air, with axial distance downstream from the nozzle (as explained in Section 3.2), and the profiles expand radially and flatten. The radial velocity gradients represent a shear flow which can induce vortices in the form of vortex rings, as explained in Appendix A.

A much weaker tangential (azimuthal) component documents that the strongly-swirling internal flow is almost fully converted into the radially directed liquid motion outside the nozzle. The swirling air-core (see Figure 1) together with the continuous liquid sheet, which carries a residual rotational energy due to liquid viscosity forces, spins out the adjacent air to a weakly swirled flow. The rotational energy of the liquid transforms into the swirled air continuum by shear forces; this is evidenced namely in the near-nozzle positions (the reddish-coloured vectors at $Z = 12.5$ mm close to the nozzle centreline in Figure 12). The tangential component of the air velocity is comparable or even larger than that of the liquid here; however, it is one order of magnitude lower than the corresponding axial and radial velocity components so that it can be neglected in further energy considerations.

A second peak in the mean liquid velocity appears at spray centreline. This central high-speed stream was found at all operating regimes, and its intensity increases with increasing Z and Δp. The air and droplet velocities near the spray centreline are well coupled, and their magnitude decreases negligibly with distance downstream. The deceleration of droplets inside the stream is much less than that in the main-stream spray. Such a phenomenon was rather unexpected as the central spray region composes only of small droplets that are low-inertial and supposed to be less affected by gravity while being more prone to decelerate by the drag force than large droplets in the main-stream spray region. This phenomenon was also found in our previous investigations of the PS sprays (Durdina et al., 2014). Santolaya et al. (2010) documented a transport of the smallest droplets to the spray core of the PS spray by the incoming airflow, and the velocities of both phases were linked in this region. This explanation is in agreement with Choi et

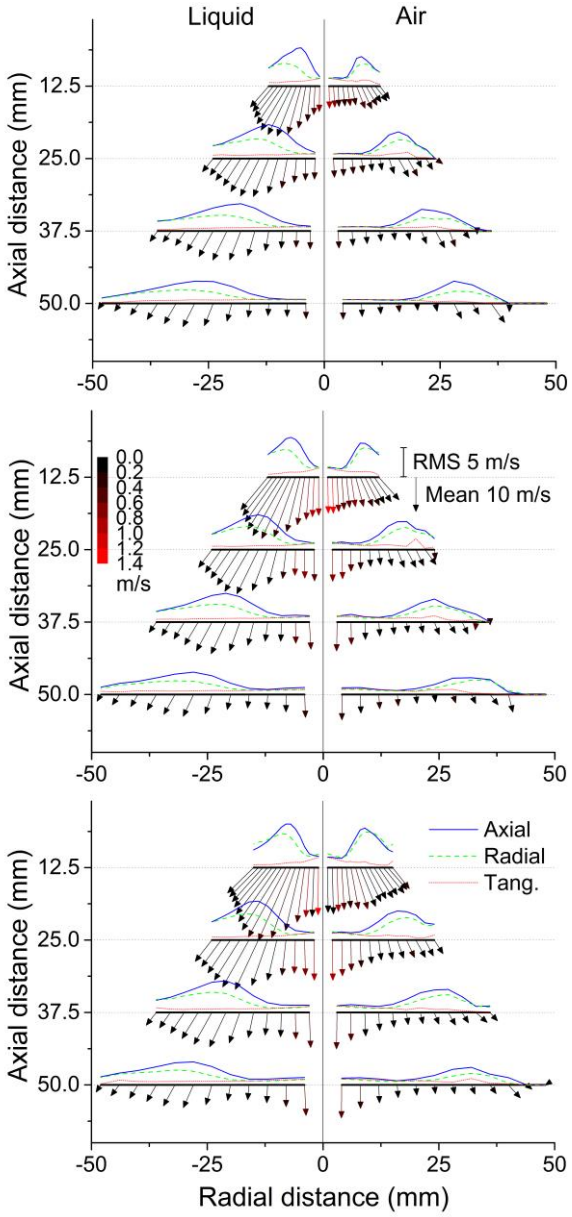

Figure 12. Spatially resolved velocity of liquid mass (left) and air (right), mean values in axial-radial directions shown as vectors colour coded according to the tangential velocity component, rms values shown as lines, $\Delta p = 0.5$, 1, 1.5 MPa (top to bottom).

al. (2002), who found out that entrained airflow accelerated the axial velocity near the spray axis and formed a vortex flow in the outer spray edge; droplets below 15 μm in diameter mostly followed this airflow. The flow field with a high centreline velocity was also identified in the hollow-cone PS sprays by Madsen (2006), and Yang et al. (2003) (without any explanation for this effect) while other works (Belhadef, Vallet, Amielh, & Anselmet, 2012; Herpfer & Jeng, 1997; J. L. Xie et al., Jun 2013) showed local minima of axial velocity in the spray centreline. Based on the current work and the previous findings, we conclude that the high-velocity local stream of small droplets is actuated by the liquid-induced central air jet which maintains its momentum downstream. The air jet is a part of a large toroidal vortex surrounding the spray, as explained in Appendix A.

The radial profiles of mean air velocity, which are flatter than the liquid velocity profiles, show an insignificant peak in the sheet direction, but only at $\Delta p = 0.5$ MPa. The air profiles at the higher pressures keep their maxima, which strengths with Δp, along the spray centreline. The velocity magnitude decreases with r and Z due to momentum transfer into the surrounding air and radial spreading of the spray cone.

The radial profiles of the axial and radial rms liquid velocity components in the individual Z positions and Δp regimes have very similar shapes with a single-peak maximum at $r \approx 0.5$–0.6. The values of the radial component are 30–50% lower than the axial component. The tangential component is, in most radial positions, much lower than the other two, and its profile is rather flat or decreasing with increasing r. The axial and radial rms profiles converge in the outer spray border ($r \approx 1$). All three rms components coincide near the spray centreline, though the tangential rms component should tend to zero in the immediate proximity of the centreline.

The profiles of all three air rms components form a plateau which spreads from the spray centreline out to $r = 0.4$–0.5, depending on Δp, with almost identical levels. These levels agree with centreline values of liquid rms velocity since the droplet size near the centreline decreases such that their $Stk < 1$ and these droplets are controlled by the airflow. The central air rms velocity values are low in comparison with local air mean velocity and also with the rms velocity outside this region. The axial and radial air rms components increase at positions $r > 0.4$–0.5 to their maxima at $r \approx 0.6$ and then continuously decrease towards the spray periphery. The axial component is 1.1 to 1.3 times larger than the radial one. Both the air and liquid rms components spread and decay with Z downstream, but this decay is less intense than in the case of the mean component.

To understand better the directional character of the velocity fluctuations, a correlation between the velocity components for a set of small ($d_p \leq 5$ μm) and large ($d_p \geq 40$ μm) droplets in an arbitrary mainstream position was documented in Figure 13. The axial-radial velocity correlation for large droplets is very strong with correlation coefficient $R^2 = 0.76$ for the linear fit. It indicates that the velocity fluctuations of the liquid mass, which induce the air fluctuations, appear mainly in the direction of the dominant spray movement (the sheet direction). Similarly, it applies to the axial-tangential velocity correlation for large droplets. Small droplets feature a weaker correlation in both cases ($R^2 = 0.26$), which suggests that the induced, highly directional, air fluctuations tend to become isotropic. This feature is in agreement with the results in Figure 12 where smaller differences between the air rms velocity components are found in comparison with the liquid ones.

The rms component of axial air velocity is of the same magnitude as the mean value while the radial and tangential rms components are even larger than their mean counterparts. The magnitude of the air fluctuations indicates that this highly turbulent flow significantly affects the small droplets in all the directions in the off-axis radial areas.

The transfer of the longitudinal velocity fluctuations of the airflow into the transversal fluctuation components affect the trajectories of small droplets and can lead to their “turbulent collisions” with large ones that are resistant to the gas fluctuations. This mechanism is most effective when the turbulent eddy size is comparable with the droplet stopping distance (Kulkarni et al., 2011); this condition is fulfilled for droplets sized between $15 < d_p < 25$ μm and the smallest eddies of the energetic range with frequencies

f = 1–2 kHz. The eddies with higher frequency do not have a sufficient magnitude (see Figure 18 below) while the eddies with lower frequencies are consistent with large droplets that feature too large *Stk*.

The droplet size-resolved velocity data (Figure 14) shows that the rms velocity at Z = 12.5 mm correlates negatively with the size. It suggests that at this position the air is already relatively turbulent due to the previous mixing with the liquid. The rms velocity of the largest droplets represents nearly the level of the original fluctuations found at the exit orifice, ≈ 4.4 m/s, and is by 30% lower than the air fluctuations. It illustrates that the air–liquid mixing contributes to the turbulent flow more than the rms fluctuations introduced by the liquid itself. These fluctuations can also increase the droplet collision rate along with the

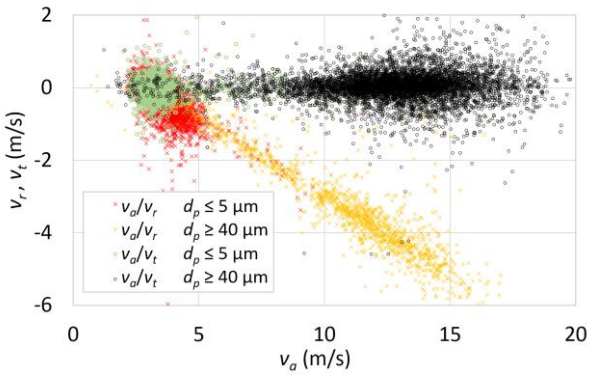

Figure 13. Velocity correlation, position Z = 37.5 mm, R = 15 mm, Δp = 1 MPa.

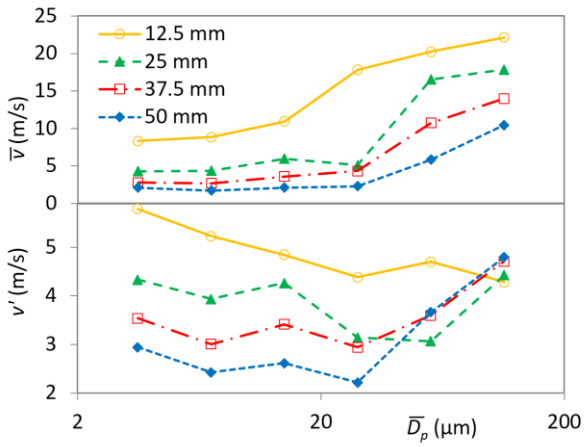

Figure 14. The size-dependent magnitude of the mean (top) and rms (bottom) velocity in individual axial positions; r = 0.56, Δp = 1 MPa.

radial dispersion of preferentially smaller droplets.

The flow field in the spray can be divided into three regions based on the airflow character found above: 1) an inner conical core at r < 0.4–0.5, with homogeneous low-level turbulence, where 1a) a central compact stream of fine droplets carried by air at moderate velocity and 1b) low-velocity droplets filling the remaining part of the inner cone appear, 2) a semi-conical part of the main spray (0.4–0.5 < r < 1) with high energy content, high turbulence levels and strongly anisotropic velocity fluctuations and 3) the low turbulence spray periphery. The air fluctuations are excited mainly in region 2 by the action of large, ballistic droplets, with *Stk* > 1 i.e. d_p > 40 µm. The mean velocity decays with axial distance downstream in regions 2 and 3 while, in the centreline area of region 1, the momentum is conserved downstream. The region 1, according to data from this work, features two-way (air ↔ droplets) to four-way (air ↔ droplets ↔ droplets) coupling while the region 2 shows a four-way coupling between the gas and liquid phases if projected into the map of flow regimes in turbulent particle-laden flows described by Elghobashi (1994).

3.6. Droplet clustering

The droplet spatial distribution features the interesting phenomena of droplet grouping or clustering. It is well evidenced in Figure 15, and it can be sensed in Figure 11 as well. The clusters appear randomly oriented, sized and spaced in the spray. The droplet aggregates are thread-shaped and are visible in the central part of the spray where a sufficient number of suitably sized droplets (10 µm < d_p < 25 µm) appear. This area, corresponding to the region 1 with homogeneous low-level turbulence (as described in Sections 3.5 and 3.7), features free shear flow. The droplet volume fraction here ranges between 10^{-4}–10^{-3} and the ratio of droplet time scale to Kolmogorov time scale is estimated to be between 300–400 depending on the axial distance from the nozzle. Such a dense spray indicates a two-way to four-way coupling (Elghobashi, 1994) with momentum transfer between the phases significant for both phases, and eventually with a

momentum exchange directly between neighbouring droplets because of their collisions. The time ratio is above the 100 limit, as given by (Elghobashi, 1994), and points out that the droplets moderately enhance turbulent production. The clusters start to form in a downstream distance ≈ 15 mm from the exit point and in random

angular positions, which

suggests that they are induced by the airflow rather than by the discharge conditions or the sheet breakup process. Droplets with high-enough inertia are flung out of vortices and tend to cluster at the vortex periphery, in the regions of low vorticity (Zonta et al., 2013). According to Sornek et al. (2000), droplets with $0.1 < Stk < 10$, especially in the outer regions of the vortex, tend to form dense groups. The rate of the droplet clustering obviously depends on the size of the vortices and is less distinct for smaller vortical structures. An analysis of interparticle arrival times from our PDA data sets shows that the clustering involves mainly the larger droplets with $d_p > 10$ μm, in agreement with the statement above. The droplet clusters formed in this way will probably not be an issue in combustion or other power and propulsion applications as the spray core contains a low fraction of the total fuel mass. It more likely just points out the intense particle–fluid interaction and the clusters can serve as "flow markers". Therefore, no further analysis of the cluster morphology, spatial distribution and development downstream is provided here. The cluster production in the relatively low-turbulent, convective part of the spray field (the whole region 1) is somewhat surprising. The randomness and uniformity of the cluster pattern, as documented in Figure 16, confirms the homogeneous and isotropic character of the turbulence field in this region. The droplet grouping was not evidenced in the region 2 which can be explained by the low concentration of appropriately sized droplets.

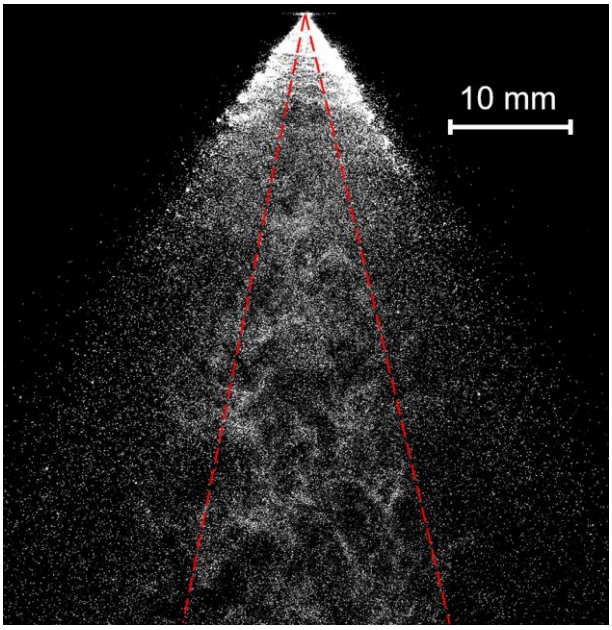

Figure 15. Droplet clustering observed in the spray core (red line demarcated area), $\Delta p = 1$ MPa. The spray is illuminated by a light-sheet going through its centreline; the image is manipulated by contrast and border enhancement.

3.7. Mean and turbulent kinetic energies in the spray

The TKE of the entrained air is quantified by the mean of the turbulence normal stresses and estimated using the velocity data of droplets with $d_p < 5$ μm[13], as

$$\mathrm{TKE} = 0.5\left[\overline{(v_x')^2} + \overline{(v_y')^2} + \overline{(v_z')^2}\right], \quad (0)$$

where v_x', v_y' and v_z' are the rms velocity fluctuations along the corresponding axes, and the overbars represent ensemble averages of the standard deviation of each component: $SD = \left(\sum_{i=1}^{n}(v_i - \bar{v})^2 / n\right)^{1/2}$. The mean kinetic energy is

[13] that are characterized by $Stk \ll 0.1$

$$\mathrm{MKE} = 0.5\left[\left(\overline{v_x}\right)^2 + \left(\overline{v_y}\right)^2 + \left(\overline{v_z}\right)^2\right]. \quad (0)$$

The TKE and the MKE values describe the distribution of the kinetic energy of the continuous phase in the spray. The radial TKE and TKE/MKE (TKE normalised by local MKE values) profiles (Figure 16) document that the TKE concentrates in the second, main stream, spray region. The radial position of its maximum corresponds to the area of maximum liquid flux. Such equivalence of the TKE radial profiles to the liquid flux profiles is due to large droplets locally, and individually, acting on the air mass thus generating a turbulent airflow. The low TKE in the first region results from the absence of large, flow inducing, droplets there.

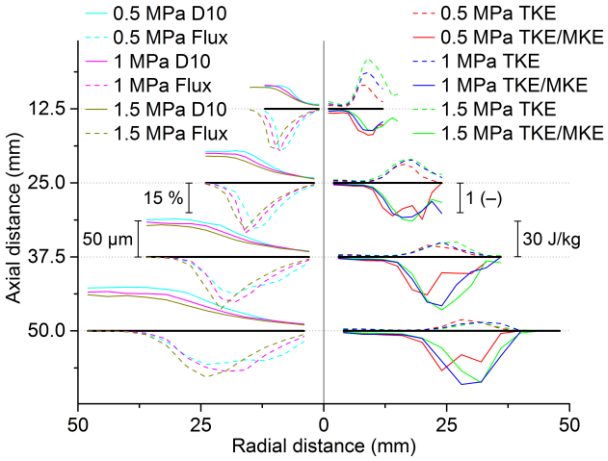

Figure 16. Spatially resolved liquid mass flux and D_{10} (left), TKE and TKE/MKE in the air (right).

The TKE maxima reduce and TKE profiles widen and shift to larger radial positions with increasing Z, so the total TKE virtually does not change. It implies that the TKE generation is in equilibrium with its dissipation downstream. The TKE varies with Δp only at $Z = 12.5$ mm; for larger Z values the shapes and levels of TKE profiles are similar among the different Δp. Such a low dependence on Δp can be explained by two opposing pressure-related factors — the droplet size and their velocity relative to the air. The interaction between droplets and the air is proportional to their relative velocity, Δv, and the projected droplet area A_p, as $F_d = 0.5\rho_g \Delta v^2 C_d A_p$. Estimating $\Delta v \sim \Delta p^{0.5}$, $C_d \sim 1/\mathrm{Re}_p \sim 1/(\Delta v \cdot d_p)$ and $A_p = \pi d_p^2/4 \sim \Delta p^{-0.6}$, when expecting that $d_p \equiv D_{32} \sim \Delta p^{-0.3}$ according to data in Table 2, results in $F_d \sim \Delta p^{0.2}$.

The radial TKE/MKE profiles feature an increase in their peak values with increasing Z, so the turbulent part of the air motion spreads less intensely in the radial direction than the mean part of flow energy. It is in agreement with above findings related to Figure 12. The TKE/MKE varies with Δp poorly, which points out that the effect of Δp on the energy transfer for both TKE and MKE is the same, as explained for TKE in the above paragraph.

The radial profiles of air and liquid MKE (not shown here) correspond to the radial profiles of mean velocity (see the corresponding vector data in Figure 12); the air MKE peaks in the spray centreline and shows local maxima also in the position of maximum liquid flux. The MKE spreads radially and reduces with Z. The liquid MKE obviously peaks in the position of maximum liquid flux for small Z and a second peak, in the spray centreline, appears with increasing Z. It decays with Z, much more intensely than the air MKE, and the dissipation is more evident with increasing Δp. The transfer of kinetic energy from the liquid into the air is intense (it relates to a relatively low droplet Stk where typically $Stk < 1$ for droplets below 30 µm, and with large droplet C_d); it augments with increasing Δp due to the contact area extension by finer droplets and widened SCA.

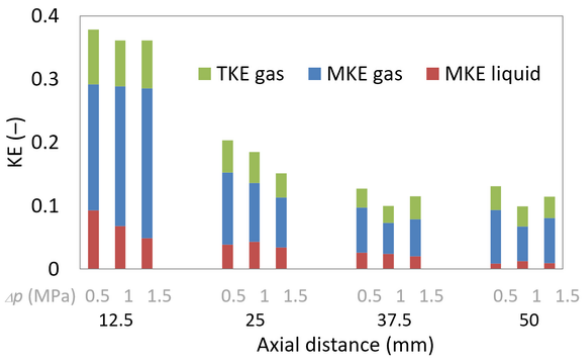

Figure 17. Specific kinetic energies of gas and liquid for individual Δp in different Z positions.

The kinetic energies of gas and liquid summed over the entire radial profiles and related to the total inlet energy are documented in Figure 17. The main obvious feature is the decay of all the energy terms with *Z*. The plot shows that the dominant part of the kinetic energy is included in the MKE of gas. However, the MKE values must be considered with care as they are rather overestimated due to the air convection induced by the mist exhaust, even though alignment was made to suppress this effect to a minimum.

The main purpose of the PS atomizer is to convert the inlet pressure energy into the increased surface tension energy of the sprayed liquid. The surface energy increment compared to the inlet energy determines to the efficiency of the atomization process, which is $\eta_a = 0.4\Delta p^{-0.66}$ (%; MPa) based on the data in Table 2. The drop down of η_a with Δp stems from the increased exchange of the liquid momentum with the air as described above and in Appendix A. The documented effectiveness of the conversion, < 0.7% for the studied range of operation regimes, is in accordance with (Bayvel & Orzechowski, 1993; Loffler-Mang & Leuckel, 1991). Its decrease with Δp also agrees with previous literature (Jedelsky & Jicha, 2014; Michalek, Peschke, & Evers, 1997; Petela, 1984; Rivette, 1996). Such a low η_a can be explained by the subthreshold interaction of the droplets with air, which does not reach the value required for the secondary breakup. The induced turbulent airflow effectively provides mixing and reposition of droplets, but a forced airflow or elevated Δp are required to increase the disrupting forces to a value sufficient for further droplet breakup.

3.8. Spectral characteristics of velocity fluctuations

The flow of the sprayed liquid mass naturally fluctuates in time and can be a subject of externally induced fluctuations and pulsations. The induced airflow follows these fluctuations and possibly transforms their character through the energy cascade. The further air–particle interactions and particle dispersion depend on the spectral properties of the flow fluctuations.

Laser-Doppler based techniques sample the spray with comparatively high temporal resolution so they can serve for estimation of the moments and spectra of the turbulent velocity fluctuations. The measured droplet concentration inside the spray cone was usually high enough to provide the data rate sufficient for such processing[14]. Therefore, the droplet velocity data were used for estimation of the power spectral density (PSD) of the velocity fluctuations. The irregularity of the sampling time interval in PDA measurements, due to the

nature of the spray, did not allow for a direct application of an FFT for the estimation of PSD of the velocity fluctuations. The slot correlation technique as described by Benedict et al. (2000) was originally tested and the PSD calculated using the Kern software (Nobach, 2002) with a setup according to Jedelsky et al. (2012). This approach produced limited results, so an interpolation method with equidistant resampling was finally applied, followed by ordinary FFT. The averaging of the plot spectra was provided over the frequency bandwidths of Δf the way that $\Delta f(f) = \pm 0.02f$ in full f range, and additionally over $\Delta f(f) = \pm 1$ Hz for 1 Hz < f < 100 Hz.

The amplitude-frequency characteristics of the PSD for the velocity fluctuations were processed for all Δp values, axial positions and all three velocity components at $r = 0.4$. Their character contains some features generally similar for all the data sets (see the log–log plot in Figure 18): the fluctuation level is high in the low-frequency band (f = 0.1–10 Hz), while for the following bandwidth, up to the cut-off frequency $f_c \approx$ 400–700 Hz, it is flat and the last band features a monotonic drop off with frequency. The PSD level in the first band does not vary with axial distance while, for the other two bands the levels systematically decrease downstream from the nozzle. The drop off in the second band corresponds to the overall decay of the rms

[14] Presuming an equal droplet distribution in space with constant concentration and mean data rate of the measurement $\dot{n}$, the intervals Δt between the droplets are distributed exponentially: $p(\Delta t) = \dot{n} \cdot e^{-\dot{n}\Delta t}$. The most probable interparticle arrival time is zero (it is practically limited by the capability of the PDA system) so information on high-frequency fluctuations is contained in the data. Nevertheless, maximum reliable frequency is $f_{max} = \dot{n}/2\pi$ according to Adrian and Yao (1987).

velocity with axial distance (see the rms velocity in Figure 12) while in the last band, rather a shift of f_c with Z occurs, instead of an amplitude variation. Note that the measured f_c loosely varies with Z due to the link between the fluctuation frequency and flow velocity as expressed by the wavenumber $k = 2\pi f / v_g$. The cut-off wavenumber k_c even increases from 153 to 778 when Z increases from 12.5 to 50 mm.

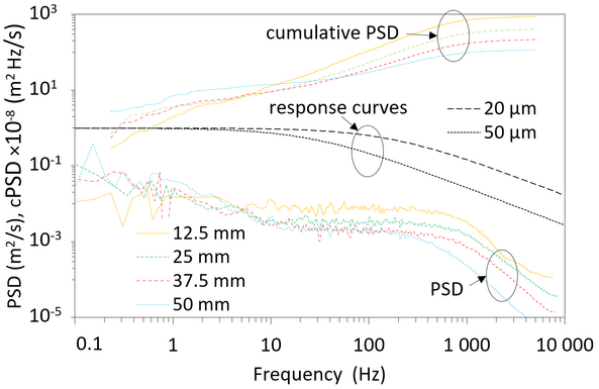

Figure 18. PSD and cumulative PSD of axial velocity fluctuations of all drop-size classes at different Z positions; $r = 0.4$, $\Delta p = 1$ MPa; theoretical response curves for 20 and 50 µm sized droplets.

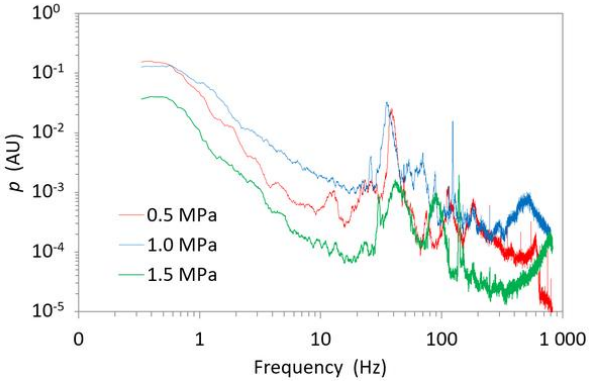

Figure 19. Frequency spectra of the pressure fluctuations in the feeding line.

The cumulative PSD in Figure 18 documents that fluctuations in a band between 100 and 1000 Hz contribute to more than 90% of the overall PSD value. The decay of the total value of fluctuations with axial distance agrees with the corresponding decay of the rms velocity.

The fluctuation spectra of the tangential velocity component (not shown due to space limitations) is similar to the other two components up to $f \approx 10$ Hz, but decreases more steeply with frequency in the upper spectral range. The effect of Δp on PSD of all the three components is insignificant. Fluctuation levels of all drop-size classes are similar up to $f \approx 10$ Hz, but large droplets in most cases show significantly larger axial and radial velocity fluctuations for $f > 10$ Hz than medium-sized and small droplets. An insignificant or even opposite effect of size was found for the tangential velocity fluctuations.

Particles of a specific size, suspended in turbulent flow, respond to the vortices and fluctuations in the fluid motion only with some approximation and their response depends on the frequency of these fluctuations. The characteristic (cut-off) frequency of the particle motion, as defined in terms of C_d, is

$$f_c = \frac{3}{8\pi} C_d Re_p \frac{\mu_g}{\rho_p d_p^2} = \frac{18}{2\pi} \frac{\mu_g}{\rho_p d_p^2} \qquad (0)$$

after Melling (1997). Figure 18 includes the response curves for the most frequent, 20 and 50 µm sized, droplets. The cut-off frequency is $f_c = 680$, 170, 27, and 6.8 Hz for 10, 20, 50, and 100 µm sized droplets, respectively. A comparison of the measured curves and theoretical responses shows a much lower theoretical f_c than the PDA based $f_c = 400$–700 Hz. Also the amplitude downtrend of the theoretical and measured response with increasing frequency over f_c differs: the theoretical particle response $\sim f^{-1}$ while the measured drop in the amplitude is typically steeper, with the exponent gradually changing from −2 to −2.4 for Z increasing from 12.5 to 50 mm and it also differs from the Kolmogorov-like constant value slope −5/3 in the inertial subrange of turbulent flows (Kaneda & Yoshida, 2004).

Measurement of pressure fluctuations in the atomizer feeding line was conducted to detect the external sources of fluctuations: pump, valves or external flow (Figure 19). This signal was dominated by low-

frequency pulsations (probably unsteadiness in the liquid delivery) with local peaks at frequencies around 40 Hz and 130 Hz that correspond to the basic and tooth frequencies of the gear pump used. Such fluctuations propagate through the atomizer and convert to velocity fluctuations of the discharged liquid. A comparison of the amplitude characteristics in Figure 18 and Figure 19 suggests that only the disturbances below 10 Hz contribute to the spray fluctuations and their energy content is very low (see the cumulative PSD curves in Figure 18).

Similarly, fluctuation phenomena in the internal flow (air core instabilities and complexities of the vortical internal flow) could contribute to deformations of the liquid sheet and disrupt its homogeneity causing fluctuation peaks in the frequency response of some spray characteristics[15].

The above findings implicate that droplet velocity fluctuations are mainly imposed during or prior to the liquid breakup phase, and the energy transfer with the air provides dumping of the fluctuations in the second frequency band (larger fluctuations of large droplets for $f > 10$ Hz compared to the small droplets) while the high-frequency fluctuations are somehow augmented (the continuous increase of k_c with Z) probably due to transformation from large to smaller vortices.

4. SUMMARY AND CONCLUSIONS

The liquid and airflow fields in spray produced by PS atomizer were investigated on an atmospheric spray bench using PDA and imaging methods.

The liquid discharged from the nozzle with rather a low nozzle efficiency of 34–41% and formed a conical sheet in the whole operational range. The near-nozzle study of the sheet breakup showed that the atomizer operated close to the transition from long- to short-wave sinuous mode instabilities that were responsible for the breakup at a length smaller than that predicted by the inviscid theoretical model. The discrepancy was explained by the internally induced flow disturbances and complexity of the internal flow while the model assumed infinitesimal disturbances imposed on the liquid film.

The sprayed droplets interact with the air through viscous drag quantified by the *Stk*; the droplets feature a wide *Stk* range with diametrically different interaction with air. Droplets with $d_p < 20$ μm match with the airflow in a short distance keeping $Stk < 1$. The velocity of droplets sized below 5 μm ($Stk << 1$) was used to estimate the local air velocity. Several requirements for suitability of the droplets for natural airflow tracings were posed and proved, such as their sufficient number and independent behaviour in the interacting droplet system. The airflow probing based on natural seeding was limited to the spray areas containing sufficient concentration of low-*Stk* particles so, for example, the air entrainment can not be discerned.

The *Stk* increases with droplet size, 20–40 μm droplets with $Stk \approx 1$ are still somewhat influenced by the airflow and establish a positive size–velocity correlation. The largest droplets (80–160 μm, $Stk > 10$) move ballistically with a high and size-independent velocity. The air-droplet interactions lead to a size-dependent droplet radial redistribution which determines the radial drop-size profile. The *Stk* varies insignificantly with the radial position but reduces with a factor of 7 for all size groups when the axial distance increases from 12.5 to 50 mm. The *Stk* systematically increases with Δp so that the values for $\Delta p = 1.5$ MPa are approximately 1.8 times greater than those for 0.5 MPa.

The liquid and gas flow fields were compared in terms of their mean and rms velocities. The radial profiles of the mean liquid velocity were self-similar amongst all the four studied axial locations and all Δp regimes with a peak close to the sheet position. The liquid velocity gradually decreases both to the spray periphery and to the centreline due to the air interaction. A second peak, which unexpectedly appears at the spray centreline, is caused by the liquid-induced air jet that acts on small droplets. The radial profiles of mean air velocity are flatter than the liquid velocity profiles. The radial profiles of the axial and radial rms

[15] Besides, the droplet velocity also interparticle arrival time, droplet diameter and volume were tested to be used for the frequency response analysis. While the PSD curves of the droplet volume shown similar features as the droplet velocity (Figure 18), PSD curves of the droplet diameter did not show any interesting information and the frequency response of interparticle arrival time (used similar way by Leboucher et al. (2014) to detect characteristic breakup frequencies) contained several isolated peaks that were attributed to harmonic frequencies of the electric net.

liquid velocity components in individual Z positions and Δp regimes are similarly shaped with a single-peak maximum at $r \approx 0.5$–0.6. The profiles of all three air rms components form a plateau which spreads from the centreline out to $r = 0.4$–0.5 with almost identical levels. These levels agree with centreline values of liquid rms velocity as the drop-size near the centreline decreases such that $Stk < 1$ and the droplets are airflow controlled. The central air rms velocity values are low in comparison with the local mean air velocity and also with the rms velocity outside this region.

The spray flow field was found spatially variable and divided into three regions according to the airflow character: 1) an inner conical core at $r < 0.4$–0.5, with homogeneous low-level turbulence, composed of a central stream of fine droplets carried by the air and low-velocity droplets in the remaining part of the inner cone, 2) a semi-conical high-energetic part of the main spray (0.4–$0.5 < r < 1$) with high turbulence and strongly anisotropic velocity fluctuations and 3) the low turbulence spray periphery. The regions featured a two-way to four-way coupling between the gas and liquid phases.

The intense transfer of kinetic energy from a liquid into the air increases the TKE and MKE of the entrained air, with the high values of kinetic energy concentrating in the second spray region. The PSD of velocity fluctuations showed that the droplet velocity fluctuates in a frequency range up to 1 kHz. The results implicate that the fluctuations in the upper-frequency band are imposed during or prior to the breakup phase, and the air dumps down the high-frequency fluctuations of small droplets.

The conditions and character of the internal flow (namely its fluctuations) control the formation of the liquid sheet, its breakup, the dropsize and SCA. The near-nozzle liquid motion, up to $Z \approx 10$ mm, follows the trajectory given by the discharge conditions, while the consequent flow is more influenced by the external gas-liquid interactions. Most of the liquid kinetic energy is transferred to the air providing the spray deceleration. The induced turbulent airflow provides mixing and radial reposition of droplets. The practical implications are that 1) a steady internal flow is needed to reduce the ID_{32} and improve the atomization efficiency and 2) an airflow control could be used to shape the spray and spatial distribution of droplet sizes. The above findings deepen the understanding of the gas-liquid interactions in PS sprays; they are relevant to engineers dealing with the processes where the gas-liquid energy transfer and droplet transport are important as well as to CFD modellers to highlight the important features of the complex two-phase flows and provide data for validation purposes.

ACKNOWLEDGEMENTS

The authors acknowledge the financial support from the project No. GA15-09040S funded by the Czech Science Foundation, the project no. CZ.1.05/2.1.00/19.0397, NETME Centre TechUp with the financial support from the Ministry of Education, Youth and Sports of the Czech Republic and project Reg. No. FSI-S-17-4444 funded by the Brno University of Technology.

APPENDIX A. AIRFLOW STRUCTURES

Figure 12 gives only a partial conception of the entire airflow field. The spatially variable sprayed droplet stream produces rich airflow structures.

The downstream droplet momentum propels the *central air stream* described in Section 3.5, which is a part of a *large stationary toroidal vortex* surrounding the spray. The airflow within the spray radially spreads and deviates from the axis in larger radial distances downstream (depicted by the diverging velocity vectors in Figure 12) and gradually turns back to close up the streamlines. We observed this vortex ring-shaped recirculating flow of the size of tens of centimetres when the mist exhaust was switched off and the ambient air was “seeded” with the small droplets produced by the atomizer. This structure was also well documented in the full scale in Figure 9a by a 2D numerical simulation of Du et al. (2017), and it was documented as a smaller cut in Figure 10.11 by Madsen (2006). Our vector plots, described in Figure 12, are in agreement with flow fields found by Santolaya et al. (2013).

Note that the form and existence of this large recirculation zone depend on the boundary conditions of the airflow and the geometry of the atomizer body and surrounding walls. The presence of the recirculation zone implicates the reposition of the small droplets from the region 2 to region 1 and the shape of their radial velocity profile. With the absence of the recirculating flow (e.g. because of an obstacle around the atomizer) the small particles would remain in region 2 which would affect the droplet size spectrum there and have consequences in combustion and other applications due to modified evaporation characteristics. It explains why in some cases the high centreline velocity in the hollow-cone PS sprays was identified (Madsen, 2006; Yang et al., 2003) while in other works not (Belhadef et al., 2012; Herpfer & Jeng, 1997; Xie et al., 2013).

The recirculating airflow consumes a significant portion of the kinetic energy of the liquid, see Figure 17. The spray-induced air entrainment rate ε (ratio of the air entrainment velocity to liquid injection velocity) can be estimated using the mean velocity values of the central air stream (the velocity vectors in Figure 12) which gives $\varepsilon \sim \Delta p^{0.16}$. The exponent of 0.16 well agrees with value 0.2 found for the dependence of the interaction force between droplets and the air in section 3.7, and it shows that the air entrainment velocity grows more steeply than the liquid velocity with increasing Δp. So the exchange of the liquid momentum with the air promotes with Δp, as shown in Figure 17, and it partially explains the drop down of η_a with Δp (Table 2 and the last paragraph in section 3.7). Note for a comparison that other researchers (Tishkoff, 1985) found for swirl chamber atomisers that ε increases linearly with liquid injection *Re* and this linear increase differs fundamentally from entrainment mechanisms for self-similar gaseous jets.

The large velocity gradients of the droplet motion in the inner and outer border of the region 2 allow a production of small vortices that are most likely formed as *vortex rings* (Chryssakis et al., 2003; Fuchimoto et al., 2009). Such vortices are probably induced by the disturbations in the discharged liquid sheet. Being energy demanding, they appear namely in the pulsating (intermittent) PS sprays (Wigley et al., 2002) and solid-cone sprays of sufficient momentum (Aggarwal et al., 1996; Park et al., 1998) while are not so frequent and intense in the continuous PS sprays. These vortices are unsteady; they develop and decay while rolling down the spray (Ma et al., 2014). It is not possible to regularly detect them using the pointwise PDA method in the case of randomly appearing vortices, but they are well documented if generated synchronously with the injection event (Wigley et al., 2002) and in particle image velocimetry (PIV) (Ma et al., 2014) and numerical (Fuchimoto et al., 2009) results (see also Figure A1 below). Another *ring-shaped vortex* may form just below the atomizer exit, outside the liquid sheet as a result of the wake produced by the spray-induced airflow around the atomizer body. This vortex was documented for example in the CFD results of Shaikh et al. (2004).

The other to note are the *randomly oriented and positioned vortices* that appear in the region 1, as described in Section 3.6. Also the results of the spectral characteristics of the velocity fluctuations, documented in Section 3.8, indirectly point out to the vortical nature of the flow within the spray cone.

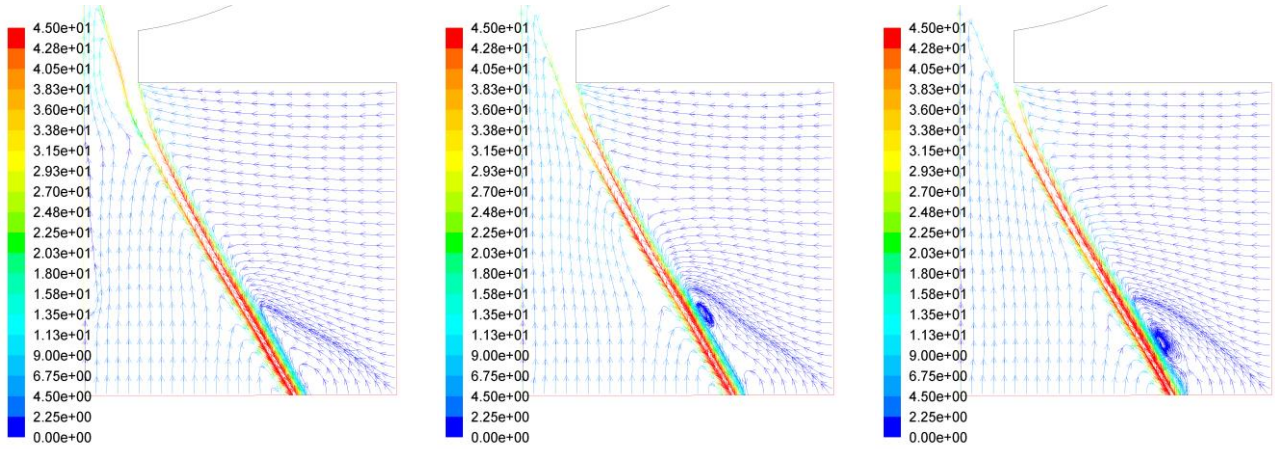

Figure A1. The discharge, liquid sheet and near nozzle flow, 2 × 2 mm area, results of CFD simulation using Ansys Fluent 17.2 (a transient 2D axisymmetric model, Volume of Fluid method, the atomizer axis is vertically positioned, and only the right part of the domain is shown), path lines colour coded by the velocity magnitude, three different time steps: 0, +33 and +44 μs; Δp = 1 MPa.

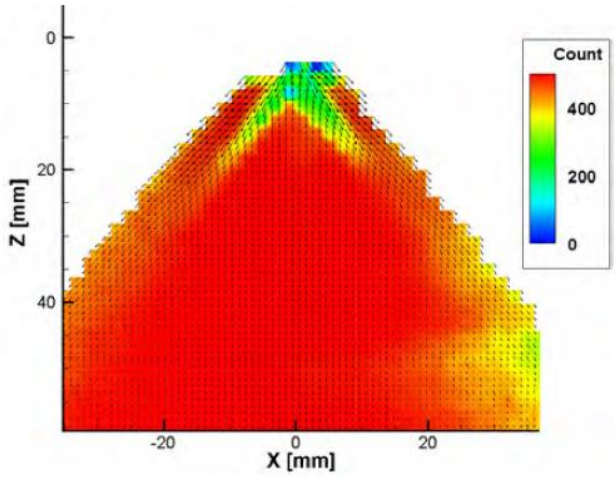

Figure A2. Vector count, mono PIV configuration with 28 mm lens, Δp = 1 MPa. Reprinted from Durdina (2012).

The continuous conical liquid sheet allows establishing a *fast rotating recirculation zone*, shaped like a deformed vortex ring, with a reversed flow near the spray centreline. The axial height of this zone is limited by the breakup distance to 3–4 mm (see Table 2 and Figure 5) and reduces with increase in Δp. The downstream distance where the sheet becomes fragmented allows the air to penetrate into the spray centre and then the *central air stream* establishes. The rotational momentum of the recirculation motion is given by the interaction of the air with the fast moving liquid film (where the discharge velocity v_0 = 22–34 m/s depending on Δp). An experimental observation of the airflow in this zone using optical diagnostics is difficult; it contains almost no particles due to the strong centrifugal forces of the rotation and also the light penetration through the liquid sheet is poor. So this zone was not well resolved in our previous PIV investigations of the PS sprays (Durdina et al., 2014). A detailed presentation of the PIV results was made by Durdina (2012); Figure A2 documents the poor PIV correlation and a low number of validated vectors noticed in the upper part of the flow field. Also, the PIV results of Du et al. (2017) in Figure 4 of their paper show the velocity vectors of poor quality with many spurious vectors in this near-nozzle

area. Our laser-Doppler Anemometry (LDA) data, Figure A3 (not shown in the main paper due to the low validation of the LDA results) confirm the reversed central airflow in $Z = 2.5$ for all Δp regimes and in $Z = 5$ mm for $\Delta p = 0.5$ MPa. This reversed flow was also documented in our recent CFD simulation of the same atomizer (Figure A1). Only a limited downstream area was simulated due to the high computing power demand. This recirculation zone just below the atomizer exit was obviously found in the CFD results of Shaikh et al. (2004), and such region with negative axial velocity was documented by Yeh (2008).

The reversed flow region might extend downstream the spray under the breakup point position if the air collection from the spray periphery is obstructed. In such a case no central air stream would form but a negative central flow would establish. We, however, did not find such a kind of inner recirculation zone in the available literature. This flow character was only proposed by Corso and Kemeny (1957), using their pressure difference measurements within the spray cone.

Based on these findings a complete idealised picture of the airflow field was composed in Figure A4. Such a complex flow field is impossible to track using point-wise experimental instruments (e.g. PDA) and difficult using planar methods (PIV). It will be very interesting to apply volumetric or tomographic experimental approaches or LES/DNS numerical simulations to verify the here described flow image, give a quantitative information on its properties and to discover its more intricate features.

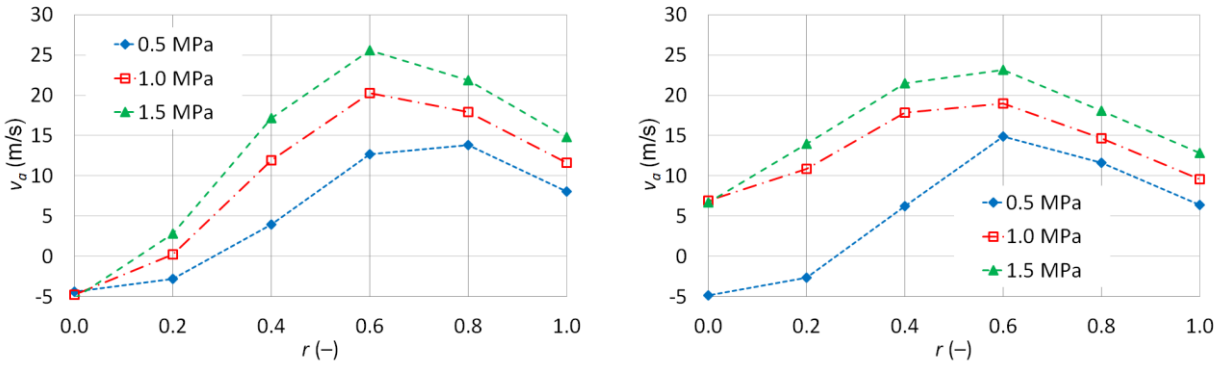

Figure A3. Mean axial velocity from LDA measurement, position $Z = 2.5$ mm (left), $Z = 5$ mm (right).

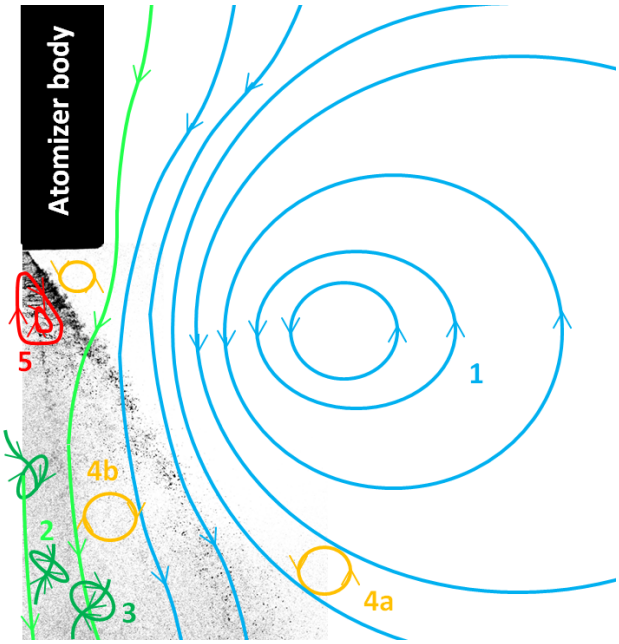

Figure A4. A scheme of airflow structures: 1) the large stationary toroidal vortex surrounding the spray, 2) the central air stream, 3) randomly oriented and positioned vortices in the region 1, 4) small vortices (vortex rings) in the inner (4b) and outer (4a) borders of the region 2, 5) fast rotating recirculation zone attached to the liquid sheet.

REFERENCES

Adrian, R. J., & Yao, C. S. (1987). Power spectra of fluid velocities measured by laser. *Exp. Fluids, 5*(1 , 1987, p.17-28.).

Aggarwal, S. K., Park T. W., & Katta, V. R. (1996). Unsteady spray behavior in a heated jet shear layer: droplet-vortex interactions. *Combust. Sci. Tech.*, 113, 429–49.

Bachalo, W. (2000). Spray diagnostics for the twenty-first century. *Atomization and Sprays, 10*(3-5).

Bai, B.-F., Zhang, H.-B., Liu, L., & Sun, H.-J. (2009). Experimental study on turbulent mixing of spray droplets in crossflow. *Experimental Thermal and Fluid Science, 33*(6), 1012-1020.

Balachandar, S., & Eaton, J. K. (2010). Turbulent dispersed multiphase flow. *Annual Review of Fluid Mechanics, 42*, 111-133.

Bates, C. J. (1994). *The effect of aperture setting on pressure atomizer phase doppler anemometry measurement.* Paper presented at the ICLASS.

Bayvel, L., & Orzechowski, Z. (1993). *Liquid Atomization*: Taylor & Francis Inc.

Belhadef, A., Vallet, A., Amielh, M., & Anselmet, F. (2012). Pressure-swirl atomization: Modeling and experimental approaches. *International Journal of Multiphase Flow, 39*, 13-20.

Benedict, L. H., Nobach, H., & Tropea, C. (2000). Estimation of turbulent velocity spectra from laser Doppler data. *Measurement Science & Technology, 11*(8), 1089-1104.

Brena de La Rosa, A., Wang, G., & Bachalo, W. (1990). *The effect of swirl on the velocity and turbulence fields of a liquid spray.* Paper presented at the ASME, 35th International Gas Turbine and Aeroengine Congress and Exposition.

Brenn, G., & Kolobaric, V. (2006). Satellite droplet formation by unstable binary drop collisions. *Physics of fluids, 18*(8), 087101.

Chinn, J. J. (2008). *The Numeric of the Swirl Atomiser*. ILASS, Como Lake, Italy.

Choi, D.-S., Choi, G.-M., & Kim, D.-J. (2002). Spray structures and vaporizing characteristics of a GDI fuel spray. *Journal of Mechanical Science and Technology, 16*(7), 999-1008.

Chryssakis, C. A., Assanis, D. N., Lee, J. K., & Nishida, K. (2003). *Fuel spray simulation of high-pressure swirl-injector for DISI engines and comparison with laser diagnostic measurements*, SAE Paper 2003-01-0007.

De Corso, S., & Kemeny, G. (1957). Effect of ambient and fuel pressure on nozzle spray angle, *Trans. ASME*, 79 (3), 607.

Dikshit, S., Channiwala, S., Kulshreshtha, D., & Chaudhari, K. (2009). *Experimental investigations of performance parameters of pressure swirl atomizer for kerosene type fuel.* Proceedings of ASME Turbo Expo 2009, Orlando, Florida, USA, 61-77.

Deng, H.-Y., Feng, F., & Wu, X.-S. (2016). Dual-Mode Linear Analysis of Temporal Instability for Power-Law Liquid Sheet. *Atomization and Sprays, 26*(4).

Domann, R., & Hardalupas, Y. (2002). *Planar Droplet Sizing for Quantification of Spray Unsteadiness*. Paper presented at the Proc. of 18th ILASS-Europe.

Dressler, J. L. (1993). *Two-dimensional, high flow, precisely controlled monodisperse drop source*: FLUID JET ASSOCIATES SPRING VALLEY OH

Du, W., Sun., Z., Lu, G., & Yu., J. (2017). The Two-Phase High-Speed Stream at the Centerline of a Hollow-Cone Spray Produced by a Pressure-Swirl Nozzle, *Industrial & Engineering Chemistry Research*, 56, 359−367.

Durdina, L. (2012). *Measurement of Spray Characteristics Using Optical Measurement Methods*. Diploma thesis, Brno University of technology. 81p.

Durdina, L., Jedelsky, J., & Jicha, M. (2014). Investigation and comparison of spray characteristics of pressure-swirl atomizers for a small-sized aircraft turbine engine. *International Journal of Heat and Mass Transfer, 78*(0), 892-900.

Eaton, J. K., & Fessler, J. (1994). Preferential concentration of particles by turbulence. *International Journal of Multiphase Flow, 20*, 169-209.

Elbadawy, I., Gaskell, P. H., Lawes, M., & Thompson, H. M. (2015). Numerical investigation of the effect of ambient turbulence on pressure swirl spray characteristics. *International Journal of Multiphase Flow, 77*, 271-284.

Elghobashi, S. (1994). On predicting particle-laden turbulent flows. *Applied scientific research, 52*(4), 309-329.

Fraser, R. (1953). Research into the Performance of Atomizers for Liquid. *Imp. Coll. Chem. Eng. Soc. J., 7*, 52-68.

Fraser, R., Eisenklam, P., Dombrowski, N., & Hasson, D. (1962). Drop formation from rapidly moving liquid sheets. *AIChE Journal, 8*(5), 672-680.

Frohn, A., & Roth, N. (2000). *Dynamics Of Droplets*. Berlin: Springer-Verlag.

Fuchimoto, T., Yanase, S., Mizushima, J., & Senda, J. (2009). Dynamics of vortex rings in the spray from a swirl injector. *Fluid Dynamics Research*, 41, 22p.

Giffen, E., & Muraszew, A. (1953). *The Atomization of Liquid Fuels*. London: Chapman & Hall Ltd.

Guo, M. (2015). *Characterization of Fuel Spray Injected by Hole-Type Nozzle into Cross-Flow Ambient*, Ph.D. Dissertation, Hiroshima University.

Herpfer, D. C., & Jeng, S.-M. (1997). Planar measurements of droplet velocities and sizes within a simplex atomizer. *AIAA journal, 35*(1), 127-132.

Horvay, M., & Leuckel, W. (1985). *LDA-measurements of liquid swirl flow in converging swirl chambers with tangential inlets.* Paper presented at the 2nd International Symposium on Applications of Laser Anemometry to Fluid Mechanics.

Horvay, M., & Leuckel, W. (1986). Experimental and theoretical investigation of swirl nozzles for pressure-jet atomization. *German chemical engineering, 9*(5), 276-283.

Jedelsky, J., & Jicha, M. (2014). Energy considerations in spraying process of a spill-return pressure-swirl atomizer. *Applied Energy, 132*(0), 485-495.

Jedelsky, J., Lizal, F., & Jicha, M. (2012). Characteristics of turbulent particle transport in human airways under steady and cyclic flows. *International Journal of Heat and Fluid Flow*.

Kaneda, Y. & Yoshida, K. (2004). Small-scale anisotropy in stably stratified turbulence. *New Journal of Physics, 6*(1), 34.

Katoshevski, D., Shakked, T., Sazhin, S. S., Crua, C., & Heikal, M. R. (2008). Grouping and trapping of evaporating droplets in an oscillating gas flow. *International Journal of Heat and Fluid Flow, 29*(2), 415-426.

Koyama, M. & Tachibana, S. (2013). Technical applicability of low-swirl fuel nozzle for liquid-fueled industrial gas turbine combustor. *Fuel* 107, 766–776.

Kulkarni, P., Baron, P. A., & Willeke, K. (2011). *Aerosol measurement : principles, techniques, and applications* (3rd ed.). Hoboken, N.J.: Wiley.

Leboucher, N., Roger, F., & Carreau, J.-L. (2014). *Atomization characteristics of an annular liquid sheet with inner and outer gas flows.* Atomization and Sprays 24(12), 1065-1088.

Lee, J., & Lee, C. (2014). Lagrangian statistics of inertial particles in near-wall turbulence. *Bulletin of the American Physical Society, 59*.

Lee, S. (1987). Particle drag in a dilute turbulent two-phase suspension flow. *International journal of multiphase flow, 13*(2), 247-256.

Lefebvre, A., & Suyari, M. (1986). Film thickness measurements in a simplex swirl atomizer. *Journal of propulsion and Power, 2*(6), 528-533.

Lecourt, R., Linassier, G., & Lavergne, G., (2011). *Detailed characterisation of a swirled air/kerosene spray in reactive and non-reactive conditions downstream from an actual turbojet injection system*. Proceedings of ASME Turbo Expo 2011, Vancouver, Canada, 185-194.

Liu, H. (2000). *Science and engineering of droplets : fundamentals and applications*. Park Ridge, N.J. Norwich, N.Y.: Noyes Publications ; William Andrew Pub.

Loffler-Mang, M., & Leuckel, W. (1991). Atomization with Spill-Controled Swirl Pressure-Jet Nozzles. *ICLASS-91, Gaithersburg, MD, USA*, 431-440.

Ma, Z. (2001). *Investigation on the Internal Flow Characteristics of Pressure-Swirl Atomiser*, Ph.D. Dissertation, University of Cincinnati, Cincinnati, OH.

Ma, H., Wu, X., Feng, F., Wang, D., Yang, Ch., & Zhuo, Ch. (2014). An experimental study on spray-induced vortex-like structures. *Experimental thermal and fluid science*, 57. 335-343.

Madsen, J. (2006). *Computational and experimental study of sprays from the breakup of water sheets.* Aalborg University.

Marchione, T., Allouis, C., Amoresano, A., & Beretta, F. (2007). Experimental Investigation of a Pressure Swirl Atomizer Spray. *Journal of propulsion and Power, 23(5)*, 1096-1101.

Melling, A. (1997). Tracer particles and seeding for particle image velocimetry. *Measurement Science & Technology, 8*(12), 1406-1416.

Mellor, R., Chigier, N., & Beer, J. (2013). *Hollow Cone Liquid Spray in Uniform Airstream.* Paper presented at the Combustion and Heat Transfer in Gas Turbine Systems, Cranfield International Symposium Series.

Michalek, D., Peschke, B., & Evers, L. (1997). Computational design of experiments for compound fuel injector nozzles. *SAE Tech Pap, Ser 971617*.

Nakayama, M., & Ohono, T. (1978). *Experimental Investigation of Atomizing Characteristics of Grooved Swirl Nozzle*, Proc. of 1st Int. Conf. on Liquid Atomization and Spray Systems (ICLASS), Tokyo.

Nobach, H. (2002). Local time estimation for the slotted correlation function of randomly sampled LDA data. *Experiments in Fluids, 32*(3), 337-345.

Park, T. W., Katta, V. R., & Aggarwal, S. K. (1998). On the dynamics of a two-phase, nonevaporating swirling jet, *Int. J. Multiph. Flow*, 24, 295–317.

Park, S. H., Kim, H. J., Suh, H. K. & Lee, C. S. (2009). Atomization and spray characteristics of bioethanol and bioethanol blended gasoline fuel injected through a direct injection gasoline injector. *International journal of heat and fluid flow*, 30 (6), 1183-1192.

Petela, R. (1984). Exergetic analysis of atomization process of liquid. *Fuel*, *63*(3), 419-422.

Poo, J., & Ashgriz, N. (1991). Variation of drag coefficients in an interacting drop stream. *Experiments in Fluids*, *11*(1), 1-8.

Rachner, M., Becker, J., Hassa, C., & Doerr, T. (2002). Modelling of the atomization of a plain liquid fuel jet in crossflow at gas turbine conditions. *Aerospace Science and Technology*, *6*(7), 495-506.

Ramamurthi, K., & Tharakan, T. (1998). Flow transition in swirled liquid sheets. *AIAA journal*, *36*(3), 420-427.

Rashad, M., Yong, H., & Zekun, Z. (2016). Effect of geometric parameters on spray characteristics of pressure swirl atomizers, *Int. J. Hydrogen Energy*, 41, 35, 15790–15799.

Rivette, S. M. (1996). Compound port fuel injector nozzle droplet sizes and spray patterns.

Rizk, N. K., & Lefebvre, A. H. (1985). Internal flow characteristics of simplex swirl atomizers. *Journal of Propulsion and Power*, *1*(3), 193-199.

Rottenkolber, G., Meier, R., Schafer, O., Wacther, S., Dullenkopf, K., & Witting, S. (2000). *Combined PDA and LDV Measurements: Phase Discrimination Inside a Spray Using Fluorescence Seeding Particles*, 10th International Symposium on Applications of Laser Techniques to Fluid Mechanics.

Rouson, D. W., & Eaton, J. K. (2001). On the preferential concentration of solid particles in turbulent channel flow. *Journal of Fluid Mechanics*, *428*, 149-169.

Sanchez, M., Castro, F., Tinaut, F., & Melgar, A. (2000). Considerations on the gas-phase velocity field in a nonevaporating diesel spray. *Atomization and Sprays*, *10*(6).

Santolaya, J., Aisa, L., Calvo, E., García, I., & García, J. (2010). Analysis by droplet size classes of the liquid flow structure in a pressure swirl hollow cone spray. *Chemical Engineering and Processing: Process Intensification*, *49*(1), 125-131.

Santolaya, J. L., García, J. A., Calvo, E., & Cerecedo, L. M. (2013). Effects of droplet collision phenomena on the development of pressure swirl sprays. *International Journal of Multiphase Flow*, *56*(0), 160-171.

Senecal, P. K., Schmidt, D. P., Nouar, I., Rutland, C.J., Reitz, R.D., & Corradini, M.L. (1999). Modeling high-speed viscous liquid sheet atomization. *International Journal of Multiphase Flow*, *25*(6–7), 1073–1097

Shaikh, S., Banaszak, U., Von Lavante, E., Cooper, D., & Yule, A. J. (2004). *CFD prediction of the Effects of Viscosity on the Internal Flow of a Scale Pressure-swirl Atomiser*. 19th ILASSEurope, Nottingham (United Kingdom), 6-8.

Sharief, R., Jeong, J., & James, D. (2000). The performance characteristics of solid-cone-spray pressure-swirl atomizers. *Atomization and Sprays*, *10*(6).

Simmons, H. C., & Harding, C. F. (1981). Some effects of using water as a test fluid in fuel nozzle spray analysis. *J Eng Power-Trans Asme*; 103(1), 118–123.

Sirignano, W. A. (2000). *Fluid dynamics and transport of droplets and sprays* (Vol. 1): Cambridge university press Cambridge.

Soldati, A., & Marchioli, C. (2009). Physics and modelling of turbulent particle deposition and entrainment: Review of a systematic study. *International Journal of Multiphase Flow*, *35*(9), 827-839.

Sornek, R. J., Dobashi, R., & Hirano, T. (2000). Effect of turbulence on vaporization, mixing, and combustion of liquid-fuel sprays. *Combustion and flame*, *120*(4), 479-491.

Sturgess, G., Syed, S., & McManus, K. (1985). Calculation of a hollow-cone liquid spray in a uniform airstream. *Journal of Propulsion and Power(ISSN 0748-4658)*, *1*, 360-369.

Takahashi, F., Schmoll, W., & Dressler, J. L. (1995). Characteristics of a velocity-modulated pressure-swirl atomizing spray. *Journal of Propulsion and Power*, *11*(5), 955-963.

Tishkoff, J. M. (1985). *Air entrainment into sprays from swirl chamber atomisers*. ICLASS-85; Proceedings of the Third International Conference on Liquid Atomisation and Spray Systems, London, England, Volume 2 (A87-13826 03-34), p. VIIC/4/1-VIIC/4/10.

Tishkoff, J. M., Hammond, D. C. Jr, & Chraplyvy, A. R. (1982). Diagnostic Measurements of Fuel Spray Dispersion, *J Fluids Engrg*, 104(3), 313-317.

Tropea, C., Yarin, A. L., & Foss, J. F. (2007). *Springer handbook of experimental fluid mechanics*. Berlin: Springer.

Villermaux, E. (2004). Unifying ideas on mixing and atomization. *New Journal of Physics*, *6*(1), 125.

Walzel, P. (1993). Liquid atomization. *Journal Name: International Chemical Engineering (A Quarterly Journal of Translations from Russia, Eastern Europe and Asia); (United States); Journal Volume: 33:1*, Medium: X; Size: Pages: 46-60.

Wang, H., McDonell, V., & Samuelsen, G. (1992). *The two-phase flow downstream of a production engine combustor swirl cup.* Paper presented at the Symposium (International) on Combustion.

Wang, X. F., & Lefebvre, A. H. (1987a). Mean drop sizes from pressure-swirl nozzles. *J Propul. Power*, 3(1), 11–18.

Wang, X. F. & Lefebvre, A. H. (1987b). Influence of ambient air pressure on pressure-swirl atomisation. *Atomizat. Spray Tech.*, 3, 209-226.

Wang, X., Chen, W., Gao, J., Jiang, D., Huang Z. (2007). Spray characteristics of high-pressure swirl injector fueled with alcohol. *Front. Energy Power Eng. China*, 1(1): 105–112.

Wigley, G., Goodwin, M. S., & Pitcher, G. (2002). *Fuel Break-up and Atomisation in the Near Nozzle Region of a GDI Injector*, IMechE, Fuel Injection Systems, Paper: L15_C610_019, 11p.

Xie, J., Gan, Z., Wong, T., Duan, F., Yu, S., & Wu, Y. (2014). Thermal effects on a pressure swirl nozzle in spray cooling. *International Journal of Heat and Mass Transfer*, *73*, 130-140.

Xie, J. L., Gan, Z. W., Duan, F., Wong, T. N., Yu, S. C. M., & Zhao, R. (Jun 2013). Characterization of spray atomization and heat transfer of pressure swirl nozzles. *International Journal of Thermal Sciences, 44*(28), 9.

Yang, J., Chen, A., Yang, S., & Huang, K. (2003). *Flow analysis of spray patterns of pressure-swirl micro atomizers.* Paper presented at the Pacific Symposium on Flow Visualization and Image Processing.

Yeh, Ch.-L. (2008). Turbulent flow simulation of liquid jet emanating from pressure-swirl atomizer. *Heat Mass Transfer*, 44: 275–280.

Yule, A., & Chinn, J. (1997). *Pressure swirl atomizer internal flow and performance*, Proceedings of the 10th annual conference on liquid atomization and spray systems ILASS, Americas, 205-209.

Yule, A., & Chinn, J. (2000). The internal flow and exit conditions of pressure swirl atomizers. *Atomization and Sprays, 10*(2), 121-146.

Yule, A. J., & Dunkley, J. J. (1984). *Atomization of Melts: For Powder Production and Spray Deposition*. USA: Oxford University Press.

Yule, A.J. & Widger, I.R. (1996). Swirl atomizers operating at high water pressure. *Int. J. Mech. Sci*., 38: 981–999.

Zhao, Y., Li, W., & Chin, J. (1986). Experimental and analytical investigation on the variation of spray characteristics along radial distance downstream of a pressure swirl atomizer. *Journal of engineering for gas turbines and power, 108*(3), 473-478.

Zimmer, L., Domann, R., Hardalupas, Y., & Ikeda, Y. (2003). Simultaneous laser-induced fluorescence and Mie scattering for droplet cluster measurements. *AIAA journal, 41*(11), 2170-2178.

Zonta, F., Marchioli, C., & Soldati, A. (2013). Particle and droplet deposition in turbulent swirled pipe flow. *International Journal of Multiphase Flow, 56*, 172-183.